buildings

MDPI

Article

Mechanical Properties of Steel Fiber-Reinforced, Recycled, Concrete-Filled Intersecting Nodes in an Oblique Grid

Jun Zhao [1,†], Feicheng Wang [2,†], Yinhong Zhu [3,*] and Bai Yang [1,*]

[1] School of Architecture and Transportation Engineering, Guilin University of Electronic Technology, Guilin 541004, China
[2] Construction Institute, Guangdong Technology College, Zhaoqing 526000, China; wangfc001230@e.gzhu.edu.cn
[3] College of Civil Engineering and Architecture, Guilin University of Technology, Guilin 541004, China
* Correspondence: zyh6130@163.com (Y.Z.); ayangbai@163.com (B.Y.)
† These authors contributed equally to this work.

Abstract: The construction of high-rise oblique grid buildings requires a large amount of concrete. To save resources, an oblique grid of intersecting nodes composed of steel outer tubes and steel fiber, recycled concrete inner tubes (OGSFRCIN) has been proposed. ABAQUS is used to study the mechanical properties of the nodes under axial pressure, accounting for the effects of six parameters: the oblique angle, the thickness of the stiffening ring, the thickness of the connecting plate, the concrete strength, the recycled aggregate replacement rate, and the steel fiber content. The results show that the oblique angle, connecting plate thickness, concrete strength, and steel fiber content significantly affect the ultimate bearing capacity of specimens. The reinforcing ring thickness has a significant effect on the evolution of lateral displacement. It is not advisable to use components with a replacement rate of 100% recycled aggregate in engineering practice because of insufficient lateral stiffness and ultimate strength. The specimen's out-of-plane displacement is tightly restricted when the connecting plate's thickness is greater than or equal to 10 mm. In practical engineering, the connecting plate and reinforcing ring thickness should not be less than 10 mm, and the recommended steel fiber content is 1.0% to 2.0%. Through the analysis of the mechanical properties of the OGSFRCIN under monotonic axial compression and reciprocating axial tension and compression loads, it can be seen that OGSFRCIN have good mechanical properties and can be applied in engineering practice. Here, the modified formulas for calculating the bearing capacity of OGSFRCIN are put forward.

Keywords: oblique grid; intersecting node; steel fiber; recycled concrete; finite element analysis; mechanical property

check for updates

Citation: Zhao, J.; Wang, F.; Zhu, Y.; Yang, B. Mechanical Properties of Steel Fiber-Reinforced, Recycled, Concrete-Filled Intersecting Nodes in an Oblique Grid. *Buildings* **2023**, *13*, 935. https://doi.org/10.3390/buildings13040935

Academic Editor: Oldrich Sucharda

Received: 12 March 2023
Revised: 27 March 2023
Accepted: 28 March 2023
Published: 1 April 2023

Copyright: © 2023 by the authors. Licensee MDPI, Basel, Switzerland. This article is an open access article distributed under the terms and conditions of the Creative Commons Attribution (CC BY) license (https://creativecommons.org/licenses/by/4.0/).

1. Introduction

With increasing land resources becoming scarce, the development of high-rise buildings is the general trend. On the premise of satisfying the safety and reliability of the structure, the structural form and materials of high-rise buildings will usher in continuous innovation [1,2]. The oblique grid structure is composed of several triangular nodes with zero degrees of freedom to resist external loads. The intersecting nodes are formed by four columns of concrete-filled steel tubes intersecting diagonally at a certain angle, which can meet mechanical requirements and control its section area. Therefore, it has good vertical bearing capacity and lateral stiffness, as well as excellent architectural aesthetic effects and mechanical characteristics. In recent years, it has had a promising future in global architectural development, and it has been used in many well-known landmarks around the world, such as the Swiss Re building in London, UK, the Hearst Tower in New York, USA, the Guangzhou West Tower and CCTV Headquarters in China, etc.

In recent years, scholars around the world have made some achievements in the research of oblique mesh. Fang et al. [3] proposed two intersecting joint structures: the

reinforced plate + lining plate node and the flange plate node and discovered that the latter has a better circumferential constraint effect on core concrete and mechanical properties than the former. Han et al. [4,5] found that, for spatially intersecting oblique grid nodes, the out-of-plane displacement of the nodes should be strictly controlled in the design, and forms such as reinforced floor beams or prestressed cables can be used. Secondly, the oblique angle leads to different failure modes, and the mechanical properties of the nodes are similar to those of concrete-filled steel tubular short columns. Guo et al. [6] studied intersecting nodes in oblique grid space and found that lateral displacement can be well constrained when the out-of-plane constraint value is 10–30 kN/mm. Zhou et al. [7] conducted quasi-static tests under axial reciprocating loads on intersecting joints to study their mechanical and hysteretic properties. Kim et al. [8] studied the mechanical properties of oblique mesh joints under lateral load and proposed the details of the joints and welding methods according to the test results. Huang et al. [9,10] proposed the calculation method of the oblique column section of a rectangular plane oblique grid structure and obtained the variation rule of the oblique angle, plane type, and mechanical properties. The oblique mesh's mechanical properties were found to be similar to those of the concrete-filled steel tube short columns. It was discovered that the oblique mesh's mechanical characteristics are comparable to those of concrete-filled steel tube short columns. Wu et al. [11] systematically evaluated the seismic performance of the perimeter diagrid concrete core (PDCC) structure, and the findings demonstrate that the PDCC structure has high performance under earthquake load and can be used as an efficient seismic resistance system. Song et al. [12] proposed an earthquake-resilient structural system called twisted diagrids with shear links (TDSL) and introduced a performance-based plastic design. TDSL systems are an attractive option for twisted buildings in earthquake zones. Shi et al. [13] carried out cyclic loading tests on five oblique grids intersecting nodes of concrete-filled steel tubes to study their failure modes and hysteretic characteristics. It was found that it is necessary to strengthen the weak parts along the horizontal intersecting line and the intersection between the node and the inclined column in the oblique grid nodes of the concrete-filled steel tube. Using the finite element program ABAQUS, Fu et al. [14] conducted a dynamic elastic–plastic time-history analysis of a high-rise building with a unidirectional oblique grid system under rare earthquakes. The results demonstrate that an oblique grid cylinder can be used as a component of the overall structure for high-rise or super high-rise buildings with a seismic fortification intensity of 7 degrees. Azari-Dodaran et al. [15] established the calculation formula of the ultimate bearing capacity of the KT intersecting joint of the double-plane pipe under the axial load at high temperatures. Nassiraei [16] established the design formula for the high-temperature axial compression capacity of T/Y intersecting joints through nonlinear regression analysis. Gao et al. [17] filled the string rod with concrete to increase the T-joints' bearing capacity and fire resistance limit, but this had a substantially detrimental effect on the performance after the fire since the damage to the concrete during the fire was irreparable. Lie et al. [18] proposed the in-plane plastic failure moment equation of K-type joints at specific positions. Wang et al. [19] established a link between the damage index range and the damage degree of oblique mesh concrete-filled steel tube columns at different performance levels, providing a critical foundation for earthquake-related economic loss assessment and restoration. Jun et al. [20,21] summarized the effects of primary stiffness-related parameters on the formation of plasticity, force distribution, and stiffness variations in oblique grid structures.

In conclusion, present research on oblique mesh intersecting nodes focuses mostly on the effect of exterior parameters and load modes on mechanical properties, whereas the peculiarities of interior core concrete are rarely reported. It is inevitable that using oblique mesh intersecting nodes in tall buildings will use up a lot of concrete. In this context, people began to study recycled aggregate, which is a new material that is mixed in a certain proportion after crushing, screening, and grading solid waste. The use of recycled aggregate is the recycling of solid waste, and the practical applicability of recycled aggregate has been confirmed [22–26]. By recycling renewable resources from construction debris,

recycled concrete technology efficiently reduces resource waste [27–33]. According to the benefits of recycled concrete in steel tubes [34–36], it is possible to fill recycled concrete in an oblique mesh with intersecting nodes. However, recycled concrete's mechanical characteristics and durability are less than those of regular concrete because of its inherent flaws. The toughening effect of steel fibers is employed to make up for the defects of recycled concrete in order to assure the safety of oblique mesh members and enhance their compressive capacity [37–44].

For the first time, this paper proposes oblique grid steel fiber-recycled, concrete-filled, intersecting nodes (OGSFRCIN) that combine steel fiber, recycled concrete, and outer steel pipe, which has the advantages of environmental friendliness and resource saving, and studies OGSFRCIN's mechanical properties and its theoretical formula of ultimate bearing capacity. The control parameters mainly include oblique angle, stiffening ring thickness, connecting plate thickness, concrete strength, recycled aggregate replacement rate, and steel fiber content. The control parameters are analyzed using ABAQUS finite element software. The influences of different control parameters on the mechanical properties of the OGSFRCIN, such as the load–displacement curve, out-of-plane displacement, Mises stress and strain, and failure position and mode, are studied. To verify the feasibility of OGSFRCIN's application in practical engineering, the mechanical properties of OGSFRCIN and oblique grid ordinary concrete-filled intersecting nodes (OGOCIN) are compared under axial compressive load and axial seismic load. Finally, the existing calculation formula for the ultimate bearing capacity of oblique grid nodes is modified by multi-parameter fitting. To provide a reliable reference for the revision of oblique grid node design, the ABAQUS modeling method and construction quality control are proposed.

2. Node Construction

The structural system of a concrete-filled steel tube (CFST) with oblique grid nodes proposed by Huang is adopted [45]. The structural form is composed of concrete-filled steel tubular columns intersecting at a certain angle in the plane. The main connecting and restraining members are the elliptical connecting plate, reinforcing ring, and lining plate. The connection mode for steel members is welding, as shown in Figure 1.

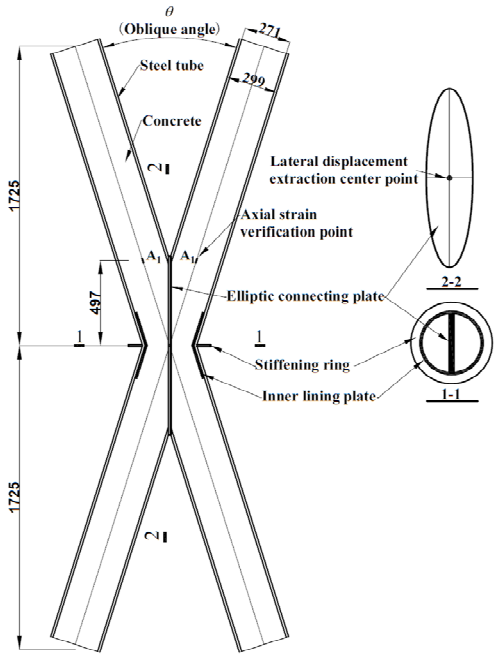


Figure 1. Node construction detail: "1" and "2" represent 1-1 and 2-2 sections, respectively.

3. Finite Element Model

3.1. Model Establishment and Boundary Conditions

In existing studies, steel components of the finite element model of an oblique grid, such as steel pipe, a reinforcing ring, and an elliptical connecting plate, are built by shell elements. The applicable conditions for shell elements [46] are as follows: The one-dimensional (thickness) dimension is much smaller than the other two-dimensional dimensions, and the deformation perpendicular to the thickness direction can be ignored. Steel parts such as reinforcing rings and elliptical node plates do not meet the above conditions, and the deformation in the thickness direction is also the focus of the research, so this modeling method has certain limitations. The loads and members are symmetrical, so Abaqus finite element analysis software is used to establish a three-dimensional solid model (C3D8R). To ensure the accuracy of the model calculation results, structural mesh technology is used to divide the models into grids. See Figure 2c–e.

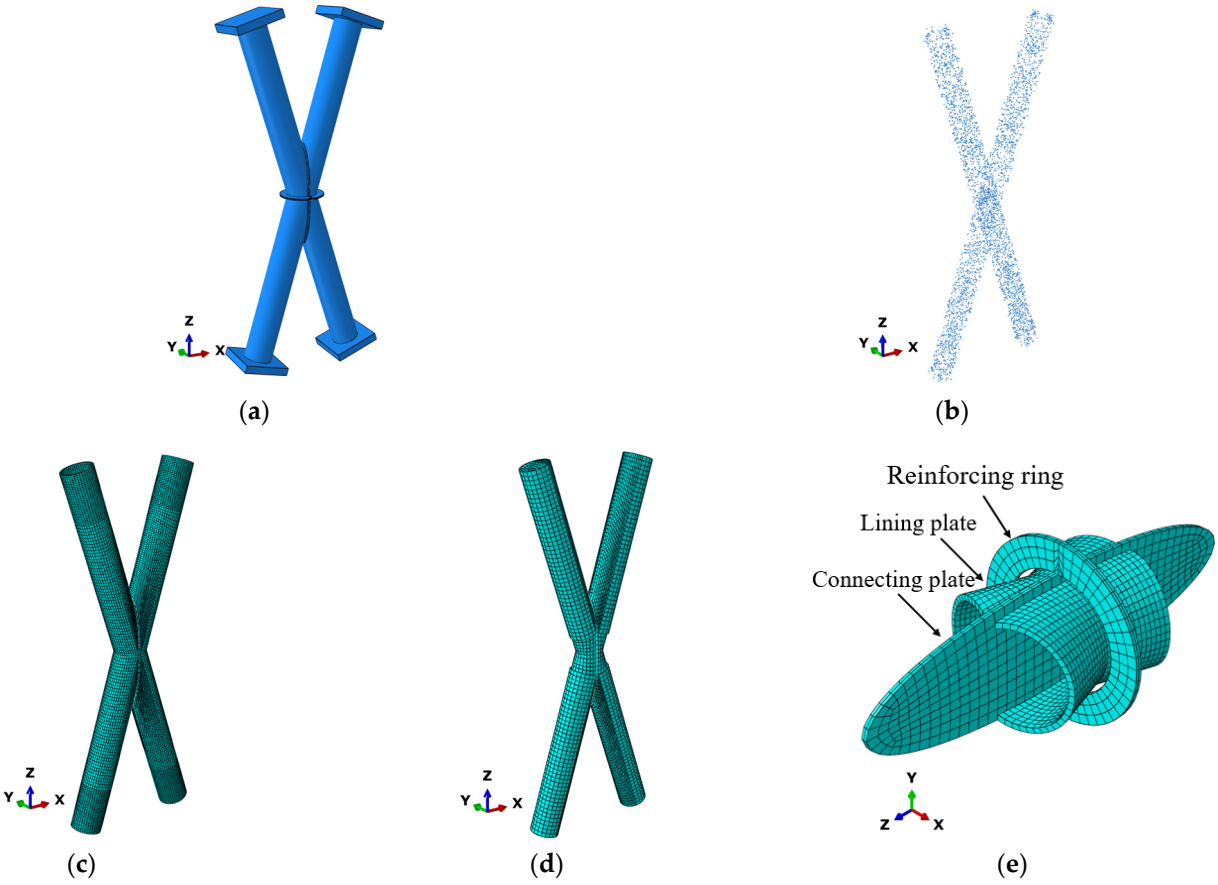


Figure 2. Node's finite element model: (**a**) overall oblique grid intersecting nodes, (**b**) steel fiber, (**c**) steel tube, (**d**) concrete, and (**e**) node area steel components.

Smooth flat steel fiber is established by the truss element, and the cross-sectional area of the steel fiber is input into the section definition. The interaction between steel fiber and concrete is the embedded region. Python script is used to set the number of steel fibers and random spatial distribution, as shown in Figure 2b. Specific mechanical parameters are shown in Table 1. In view of the fact that the concrete-filled steel tube member is prone to buckling damage near the bottom of the column in the test, grid encryption is carried out on the 450 mm area of the bottom of the steel tube. Because there exists a cohesive slip between steel pipe and concrete in the tangential direction, a cohesive element is used to simulate the cohesive slip effect, and a hard contact is used in the normal direction to prevent the penetration of the element. In the actual situation, the two steel pipe columns on the same

side of the connecting plate are welded by groove, and the nodes are welded by lining pipe with the upper and lower oblique grid columns. Therefore, the contact between all steel parts is set as a tie constraint in the model. The axial pressure displacement along the axis of the steel tube is applied to the top of the steel tube, and the reference points are established for the steel tube and the core concrete to extract the load–displacement curves, respectively. The bottom end of the steel pipe is completely fixed by ENCASTRE. Component failure can be considered when local buckling or large lateral deformation occurs.

Table 1. Shape parameters and mechanical properties of steel fibers.

d_f (mm)	l_d (mm)	Length–Diameter Ratio	Density (g/cm^2)	f_{st} (MPa)	E_{st} (MPa)
18	0.55	37.73	7.8	4500	200

Notes: d_f is the equivalent diameter of steel fiber, l_d is the length of steel fiber, f_{st} is the tensile strength of steel fiber, and E_{st} is the elastic modulus of steel fiber.

3.2. Constitutive Parameters of Material and Cohesive Force Element

3.2.1. Constitutive Model of Recycled Concrete

Because the performance defects of recycled concrete in the elastic stage are not reflected, and the stress–strain curve is the same as that of ordinary concrete, the uniaxial state of ordinary concrete is adopted in the rising stage of the stress–strain curve; for the descending section, due to the reduced elasticity, high deformation modulus, and high brittleness of recycled concrete, the curve drops sharply compared with ordinary concrete. The curvature coefficient, considering the influence of recycled aggregate replacement rate, is introduced. In this paper, the revised uniaxial compression stress–strain relation formula of steel tube-restrained core concrete [47,48] is used, as shown in Equations (1)–(8) and Figure 3a:

$$y = \begin{cases} 2x - x^2; (x \le 1) \\ \frac{x}{\psi\beta(x-1)^2+1}; (x > 1) \end{cases}, \quad (1)$$

$$x = \frac{\varepsilon}{\varepsilon_0};\ y = \frac{\sigma}{\sigma_0};\ \psi = 2 + 1.5\delta_R, \quad (2)$$

$$\beta = \left(2.36 \times 10^{-5}\right)^{(0.25+(\theta-0.5)^7)} \times f_{c,R} \times 0.5 \ge 1.2, \quad (3)$$

$$\sigma_0 = \left[1 + \left(-0.054\theta^2 + 0.4\theta\right)\left(\frac{24}{f_{c,R}}\right)^{0.45}\right] f_{c,R}, \quad (4)$$

$$\theta = \frac{A_s f_y}{A_c f_{c,R}}; f_{c,R} = 0.8 f_{cu,R}, \quad (5)$$

$$\varepsilon_0 = \varepsilon_{cc} + \left[1400 + 800\left(\frac{f_{c,R}}{24} - 1\right)\right]\theta^{0.2}, \quad (6)$$

$$\varepsilon_{cc} = 1900 + 800\theta^{0.2}, \quad (7)$$

$$\frac{f_{cu,R}}{f_{cu,0}} = -0.4247{\delta_R}^3 + 0.2486{\delta_R}^2 + 0.2486\delta_R + 1, \quad (8)$$

where $f_{cu,R}$ is the concrete cube's compressive strength under different recycled aggregate replacement rate; $f_{cu,0}$ represents the cube's compressive strength when the replacement rate of recycled aggregate is 0%; $f_{c,R}$ is the axial compressive strength of cylinder under different recycled aggregate replacement rate; f_y is the yield strength of steel, 271.25 MPa; A_s and A_c are the cross-section area of steel pipe and concrete, respectively; ψ is the influence coefficient of replacement rate of recycled aggregate; δ_R is the replacement rate of recycled aggregate; θ is the restraint effect coefficient.

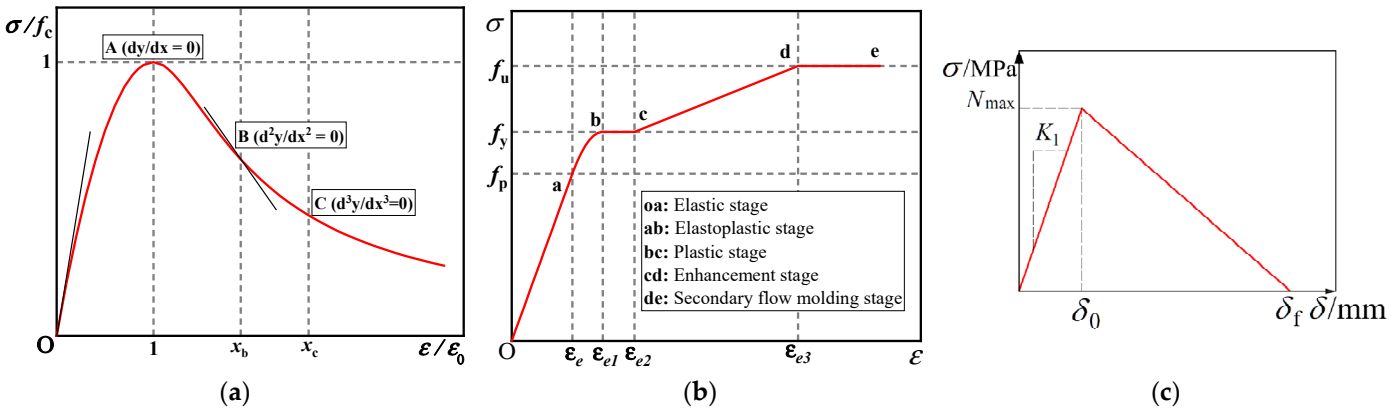


Figure 3. Constitutive curve: (**a**) uniaxial compression constitutive of recycled concrete, (**b**) simplified secondary flow constitutive of steel, and (**c**) cohesive constitutive.

3.2.2. Steel Constitutive Relation

Steel pipe is generally made of low-carbon steel. As an elastic–plastic material, von Mises' yield criterion strength theory is adopted [49]. The five-segment quadratic plastic flow model should be adopted for the constitutive relationship, as shown in Equations (9)–(12) and Figure 3b.

$$\sigma_i = \begin{cases} E_s\varepsilon_s;\varepsilon_s<\varepsilon_e \\ -A{\varepsilon_s}^2 + B\varepsilon_s + C;\varepsilon_e \le \varepsilon_s \le \varepsilon_{e1} \\ f_y;\varepsilon_{e1} \le \varepsilon_s \le \varepsilon_{e2} \\ f_y\left[1+0.6\frac{\varepsilon_i-\varepsilon_{e2}}{\varepsilon_{e3}-\varepsilon_{e2}}\right];\varepsilon_{e2} \le \varepsilon_s \le \varepsilon_{e3} \\ f_u;\varepsilon_{e3}<\varepsilon_s \end{cases}, \tag{9}$$

$$A = \frac{0.2f_y}{(\varepsilon_{e1}-\varepsilon_e)^2}, \tag{10}$$

$$B = 2A\varepsilon_{e1}, \tag{11}$$

$$C = 0.8f_y + A{\varepsilon_e}^2 - B\varepsilon_e, \tag{12}$$

where σ_i is equivalent stress (von Mises yield criterion), E_s is the elastic modulus, ε_e is yield strain, ε_{e1} is strain corresponding to starting point of reinforcement, ε_{e2} is strain corresponding to ultimate tensile strength, f_y is the yield strength, and f_u is ultimate tensile strength. Detailed parameters are shown in Table 2.

Table 2. Steel strength.

Steel Type	Model Number	Elastic Modulus E_s/Mpa	Yield Strength f_y/Mpa	Ultimate Strength f_u/MPa
Outer steel pipe	20 #	2.06×10^5	271.25	448.75
Elliptic connecting plate	20 #	2.06×10^5	271.25	448.75
Backing plate	-	2.00×10^{10}	-	-

3.2.3. Cohesive Constitutive Model

A cohesive element contact model is introduced to simulate the cohesive slip between the core concrete and steel [50]. See Figure 3c. In the figure, $N_{\max}$ is the peak tensile strength; that is, the peak bond strength between core concrete and steel. The peak bond strength [51] τ_u is calculated as shown in Equation (13), where L/D is the length–diameter ratio of steel

pipe, K_1 is the initial stiffness of the cohesive element interface, δ_0 is the corresponding displacement at the beginning of damage, and δ_f is the displacement when the element fails completely. In this paper, 0.001 mm and 0.002183 mm are taken, respectively.

$$\tau_u = \left(0.0336 + 0.0141R - 0.0028\left(\frac{L}{D}\right)\right) f_{cu,R}. \quad (13)$$

3.3. Reliability Verification of Finite Element Model

Components in the literature [40] are selected for verification. The detailed dimensions of the components are shown in Figure 1. The oblique angle is 35°, and the concrete strength grade is C60. Figure 4a shows the comparison between the test curve and the finite element curve. In the load–displacement curve, the axial displacement is the displacement of the top end of the steel pipe along the axial direction of the steel pipe. As can be seen from the figure, the evolution law between the load–displacement curve of the test and the finite element model is similar. The initial stiffness of the curve is almost the same, but the stiffness of the test curve is slightly larger, and the stiffness of the curve decreases when the load is about 5000 kN. The main reason for the fluctuation of this stiffness is that the concrete in the actual situation is heterogeneous, and there may be a few cracks and holes. However, the stiffness of the elastic section of the finite element model is almost a straight line, which is different from the actual situation. The concrete in the model is a three-dimensional homogeneous entity, which causes this difference. However, the ratio of the finite element model limit load to the test limit load is 1.0782, with a small difference. However, the displacement corresponding to the test limit load is slightly larger.

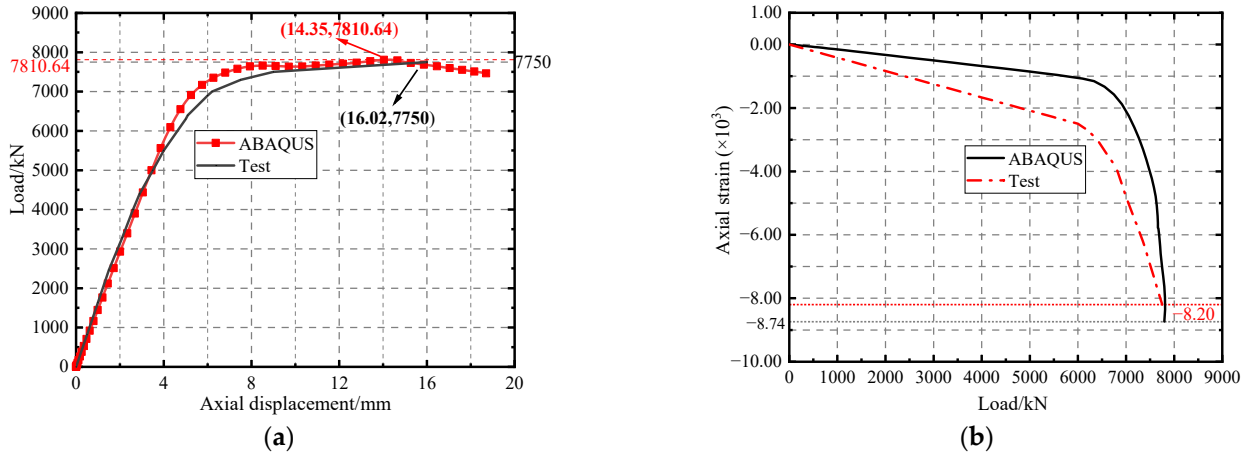
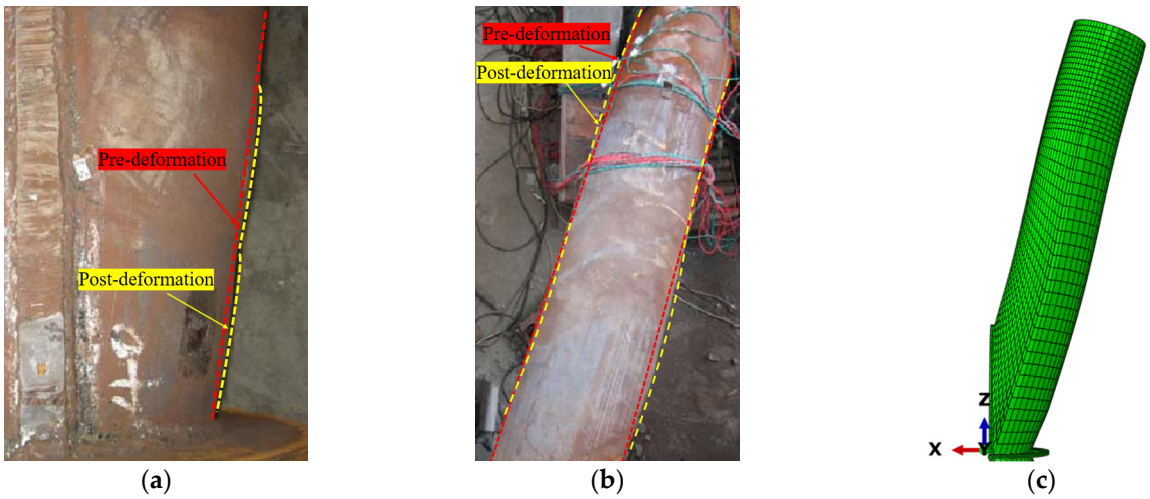


Figure 4. Comparison between test curve and finite element curve: (**a**) load displacement curve and (**b**) load-axial strain curve.

It can be seen from Figure 4b that the load–strain curves of the test and finite element have similar evolution rules, but the stiffness of the elastic section of the test curve is smaller than that of the finite element curve. This is mainly due to the difference between the concrete test and the finite element. Secondly, the load applied along the axial direction in the experiment process cannot guarantee no eccentricity, and eccentricity will cause an additional bending moment, which will weaken the mechanical properties of oblique grid nodes. The ratio of the axial peak strain of the finite element model to the axial peak strain of the test is 1.0659, and the difference is also small. To sum up, the test is in good agreement with the curve law of the finite element and related values.

Figure 5 shows the comparison of failure modes between the finite element model and the test component. It can be seen from the figure that the failure modes of the test members are mainly the microbuckling of steel pipes at a certain distance from the reinforcement ring in the node area and buckling failure of steel pipes in the non-node area. The failure modes of the members in the finite element model are in good agreement with the test

phenomena. To sum up, the finite element model based on cohesive contact elements used in this paper is in good agreement with the experimental results and phenomena and can well reflect the interaction between members of oblique grid nodes.



(**a**) (**b**) (**c**)

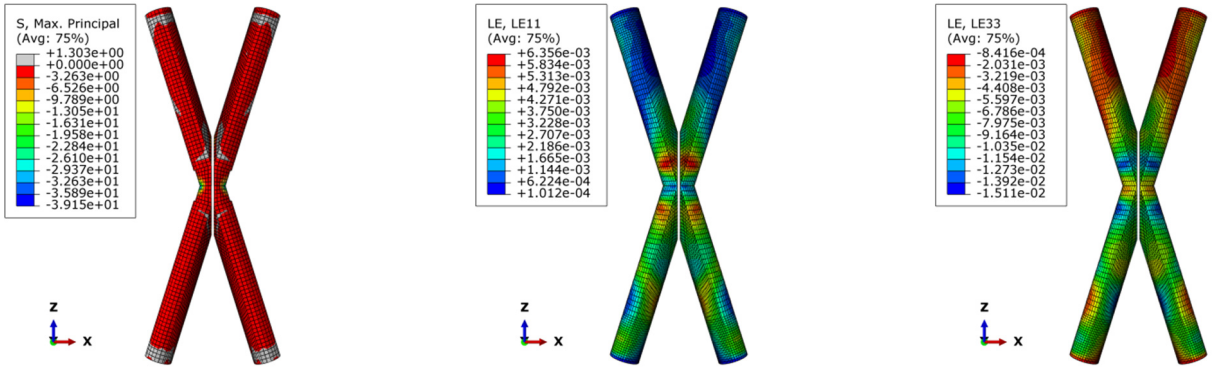
Figure 5. Comparison of failure modes between finite element model and test component: (**a**) bulging damage of steel pipe in node area, (**b**) bending failure, and (**c**) failure pattern of FEM.

3.4. Analysis of Finite Element Results

Figure 6 shows the nephogram of related parameters for components. From the figure, it can be seen that most areas of concrete are under three-dimensional compression, especially the compressive stress in the node area, which reaches the maximum value, indicating that the concrete in the node area is well constrained by the reinforcing ring, the inner lining plate, and the connecting plate. After the concrete is subjected to a large pressure load, it expands circumferentially. Because of the hoop effect of the steel pipe, the hoop strain of the steel pipe in the node area is positive, and the axial strain is negative, as shown in Equations (14) and (15): α is 1/2 oblique angle, LE_h is hoop strain, and LE_z is axial strain. The steel pipe is under axial compression and circumferential tension. It shows the good performance of restrained concrete.

$$LE_h = LE11\cos\alpha + LE33\sin\alpha, \tag{14}$$

$$LE_z = LE11\sin\alpha + LE33\cos\alpha. \tag{15}$$



(**a**) (**b**) (**c**)

Figure 6. Related cloud images: (**a**) concrete (maximum principal stress), (**b**) steel pipe (X-direction strain), and (**c**) steel pipe (Z-direction strain).

4. Parameter Setting

Considering the influence of six parameters, such as oblique angle, the thickness of the reinforcing ring, the thickness of the connecting plate, the replacement rate of recycled aggregate, fiber content, and concrete strength, on the mechanical properties of fiber-reinforced concrete oblique grid nodes, a control group specimen is designated, and the rest specimens change one parameter in turn on the basis of this specimen so as to explore the law of the influence of a single variable on the mechanical properties. See Table 3 for specific parameter settings.

Table 3. Specimen parameter settings.

Parameter Name	Oblique Angle	Thickness of Reinforcing Ring/mm	Thickness of Connecting Plate/mm	Aggregate Replacement Rate/%	Steel Fiber Content/%	Strength of Concrete/MPa
Standard group	35°	14	28	70	1.0	60
Change group	50°	00	05	00	0.0	30
	70°	05	10	30	0.5	80
	90°	10	20	50	1.5	100
				100	2.0	

5. Results

The load–displacement curve can well reflect the evolution process of members from stress to failure, and the axial displacement–lateral displacement curve can well reflect the out-of-plane displacement of the center section of the elliptical connecting plate during the loading process. The extraction point of lateral displacement is shown in Figure 1, and it can be used to determine whether members have significant deformation and failure. In addition, von Mises stress, PEEQ (equivalent plastic strain), DAMAGEC (concrete compression damage), and other parameters are also important mechanical performance indices of the oblique grid finite element model. Detailed results are shown in Table 4.

Table 4. Main results of finite element analysis.

Control Parameters	Name of Specimen	f_u/kN	δ_n/mm	δ_c/mm	σ_m/Mpa	σ_c/Mpa	k_c	μ	ξ
Standard group	A35-H14-L28-R70-r1.0-C60	7236.01375	6.809	2.24449	319.4	63.38	1.173	0.8293	3.8203
Oblique angle	A50-H14-L28-R70-r1.0-C60	6991.72583	5.747	16.355	**446.1**	**84.07**	1.133	0.8378	4.3533
	A70-H14-L28-R70-r1.0-C60	7247.85478	6.253	38.9845	**448.8**	**70.81**	1.175	0.8232	4.0039
	A90-H14-L28-R70-r1.0-C60	6553.98520	5.738	1.04889	321.3	**70.14**	1.062	0.8877	4.3684
Thickness of reinforcing ring	A35-H00-L28-R70-r1.0-C60	7227.14603	6.541	7.65638	**328.3**	85.90	1.172	0.8371	3.8247
	A35-H05-L28-R70-r1.0-C60	7320.86941	7.100	7.29164	318.4	**89.58**	1.1867	0.8324	3.5197
	A35-H10-L28-R70-r1.0-C60	7273.08419	6.807	3.9857	**331.5**	86.78	1.179	0.8416	3.6749
Thickness of connecting plate	A35-H14-L05-R70-r1.0-C60	5948.96577	17.862	5.09543	**448.8**	117.5	0.964	0.8905	1.3867
	A35-H14-L10-R70-r1.0-C60	6600.43058	6.265	1.26429	**447.7**	92.39	1.070	0.8803	3.9914
	A35-H14-L20-R70-r1.0-C60	6592.34037	13.216	2.3313	**448.1**	**121.3**	1.069	0.8828	1.9044
Aggregate replacement rate	A35-H14-L28-R00-r1.0-C60	7689.63622	7.359	0.42633	328.48	**103.1**	1.2465	0.8573	3.3921
	A35-H14-L28-R30-r1.0-C60	7502.58422	7.360	4.09687	327.2	**94.80**	1.216	0.8487	3.5256
	A35-H14-L28-R50-r1.0-C60	7369.37741	6.806	3.77469	327.6	87.22	1.195	0.8445	3.6682
	A35-H14-L28-R100-r1.0-C60	6488.53992	10.620	2.15318	**309.6**	**62.33**	1.052	0.8396	2.3512
Steel fiber content	A35-H14-L28-R70-r0.0-C60	7021.99553	6.780	3.38474	326.0	**80.23**	1.138	0.8405	3.6687
	A35-H14-L28-R70-r0.5-C60	7132.26716	6.805	5.84078	325.9	83.66	1.156	0.8388	3.6680
	A35-H14-L28-R70-r1.5-C60	7345.427196	6.814	5.92158	325.4	90.18	1.191	0.8385	3.6681
	A35-H14-L28-R70-r2.0-C60	7460.76856	6.820	4.24676	324.5	93.68	1.209	0.8368	3.6683
Strength of concrete	A35-H14-L28-R70-r1.0-C30	6219.89703	6.535	1.19423	317.4	58.46	1.300	0.8514	3.8274
	A35-H14-L28-R70-r1.0-C80	7668.49790	6.794	9.46725	321.2	**110.3**	1.081	0.8123	3.6800
	A35-H14-L28-R70-r1.0-C100	8261.81744	8.096	4.4975	337.5	**151.3**	1.031	0.8358	3.0878
Comparison group	A35-H14-L28-R30-r2.0-C60	7699.87340	13.081	5.5950	**330.2**	**108.1**	1.248	0.8413	3.440
	A35-H14-L28-R00-r0.0-C60	7810.63980	14.347	4.4840	**302.6**	**120.8**	1.266	0.8668	3.485

Table 4 shows the main results of finite element analysis, in which "A35-H14-L28-R70-r1.0-C60" is the standard group, where A is the oblique angle, H is the thickness of

reinforcing ring (mm), L is the thickness of the connecting plate (mm), R is the replacement rate of recycled aggregate (%), r is the steel fiber content (%), and C is the cubic compressive strength of concrete (MPa). δ_n is the displacement corresponding to the ultimate load, δ_c is the extreme value of out-of-plane displacement, and σ_m is the von Mises maximum value of steel parts with oblique grid structure. Bold indicates that the maximum value occurs in the node area, while not bold indicates that it occurs in the non-node area. σ_c is the von Mises maximum value of the core concrete of oblique grid structure, and the bold definition is the same as σ_m. The calculation model of the energy consumption factor μ [52] is shown in Figure 7, which can reflect the relationship between energy absorption and energy consumption of oblique grid nodes, and has the meaning of a global variable. Its expression is shown in Equation (16).

$$\mu = \frac{S_{\mathrm{OEFG}\delta_u}}{f_u \delta_m}, \tag{16}$$

where $S_{\mathrm{OEFG}\delta_u}$ is the area enclosed by the load–displacement curve and the abscissa, as shown in Figure 7. f_u is the ultimate load, and δ_m is the ultimate displacement.

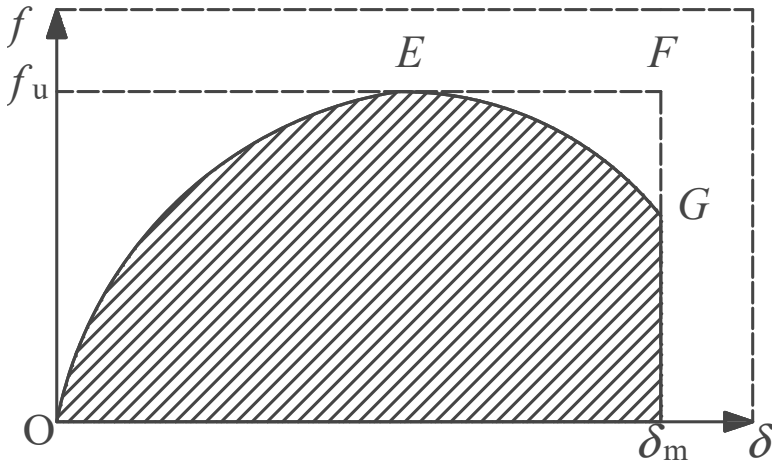


Figure 7. Calculation model of energy dissipation factor.

ξ is the ductility coefficient, and its expression is:

$$\xi = \frac{\delta_u}{\delta_n}, \tag{17}$$

where δ_u generally takes the displacement corresponding to the peak load when the load drops to 0.85 times the peak load, but since the bearing capacity of most specimens does not drop to 0.85 times the peak load, the ultimate displacement is taken and δ_n is the displacement corresponding to the peak load. In order to directly reflect the mutual compensation between steel pipe and recycled concrete, k_c is introduced as the strength improvement coefficient [53], as shown in Equation (18).

$$k_c = \frac{f_u}{f_{u0}}. \tag{18}$$

f_u is the ultimate load of the specimen,

$$f_{u0} = A_s f_y + A_c f_{c,R}. \tag{19}$$

A_s and A_c represent the section areas of steel pipe and concrete, respectively.

The load–displacement curve and axial–lateral displacement curve of the specimen are shown in Figures 8 and 9, respectively. To directly reflect the distribution of load between

steel pipe and concrete, the load–displacement curve is divided into a total displacement curve (Total) and a core concrete partial displacement curve (RAC).

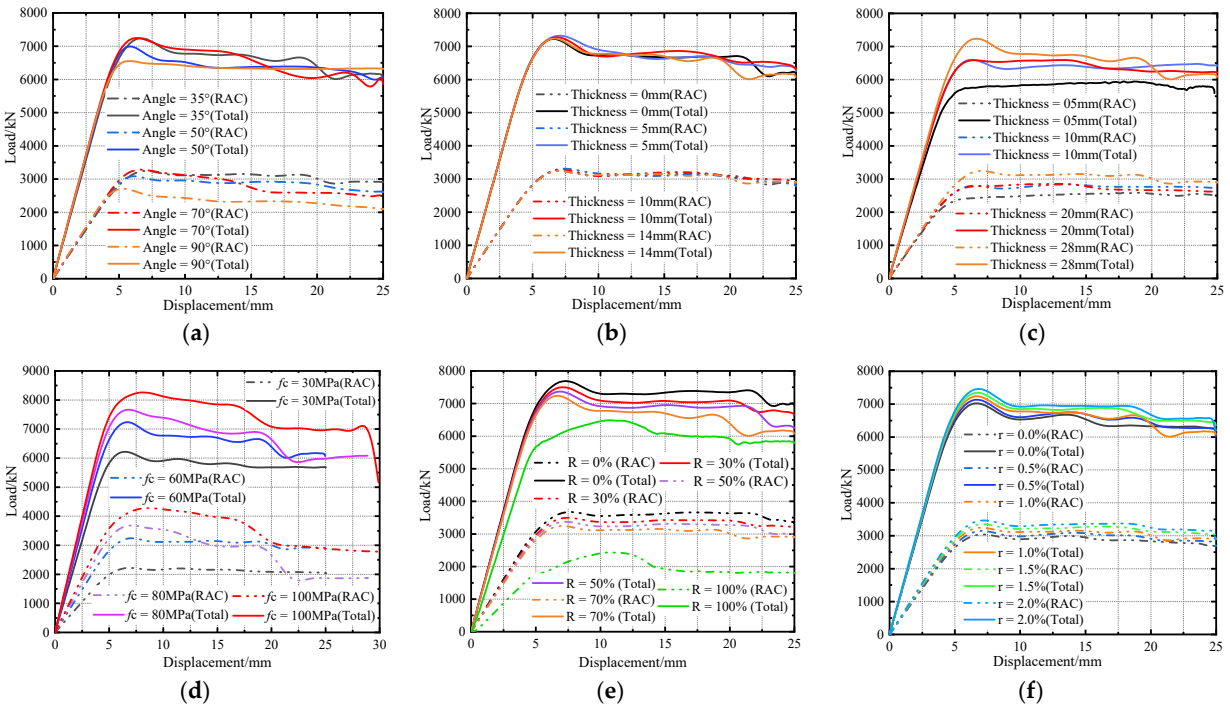


Figure 8. Load–displacement curve: (**a**) oblique angle, (**b**) thickness of reinforcing ring, (**c**) thickness of connecting plate, (**d**) concrete strength, (**e**) recycled aggregate replacement rate, and (**f**) fiber content.

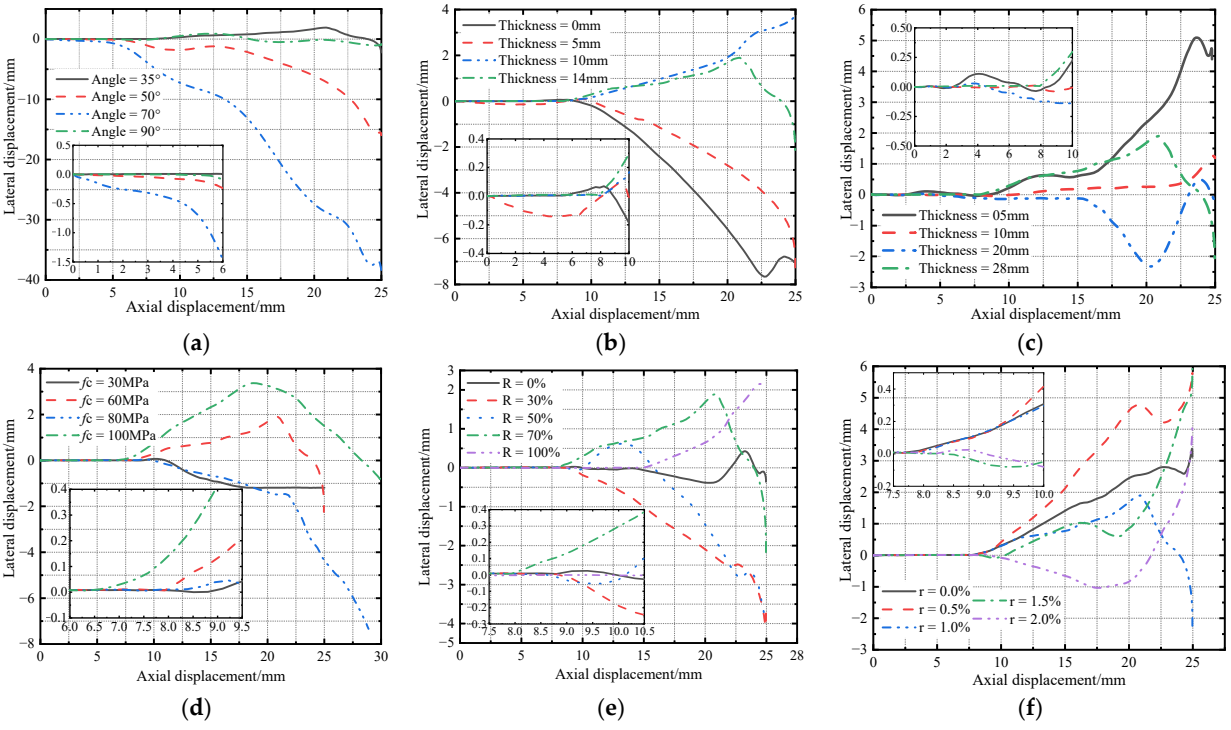


Figure 9. Axial displacement–lateral displacement curve: (**a**) oblique angle, (**b**) thickness of reinforcing ring, (**c**) thickness of connecting plate, (**d**) concrete strength, (**e**) recycled aggregate replacement rate, and (**f**) fiber content.

6. Discussion

6.1. Oblique Angle

According to the load–displacement curve in Figure 8a, the curves of oblique grid specimens with different angles have similar evolution rules. The peak load of specimens with an oblique angle of 35° is the largest, while that of specimens with an oblique angle of 90° is the smallest. The specimens with oblique angles of 35° and 70° have similar peak loads and residual loads, but the latter's load–displacement curve decreases rapidly after the peak value, and the residual load is small. It can be seen from Figure 9a that its lateral displacement began to occur when the axial displacement was less than 5 mm, and it developed nonlinearly to 38 mm, eventually causing local buckling and lateral instability failure. Second, the specimen with an oblique angle of 50° has a large lateral displacement, whereas the specimen with oblique angles of 35° and 90° develops steadily and has a small value. This is mainly because the ultimate load of the latter is small, and failure occurs without large out-of-plane deformation.

Figure 10 shows the local von Mises stress diagram of the oblique-angle specimen. The oblique angle has a significant influence on the von Mises stress of the connecting plate and the reinforcing ring in the oblique grid. When a specimen with an oblique angle of 35° fails, the von Mises stress is less than the yield strength, indicating that the specimen has a good force transmission function, and the von Mises stress of the reinforcing ring is still less than the yield strength, indicating that the component is still in the elastic stage and has a large strength margin. However, the von Mises stress values of other specimens are all large, the von Mises stress of the specimen with an oblique angle of 50° has reached the ultimate strength at the contact position between the connecting plate and the reinforcing ring, and the von Mises stress of the reinforcing ring is also large, showing uneven distribution along the zoy plane. However, the plastic deformation area of the specimen with an oblique angle of 90° is larger than that of other specimens, mainly in the middle area of the connecting plate and the contact position between the reinforcing ring and the connecting plate.

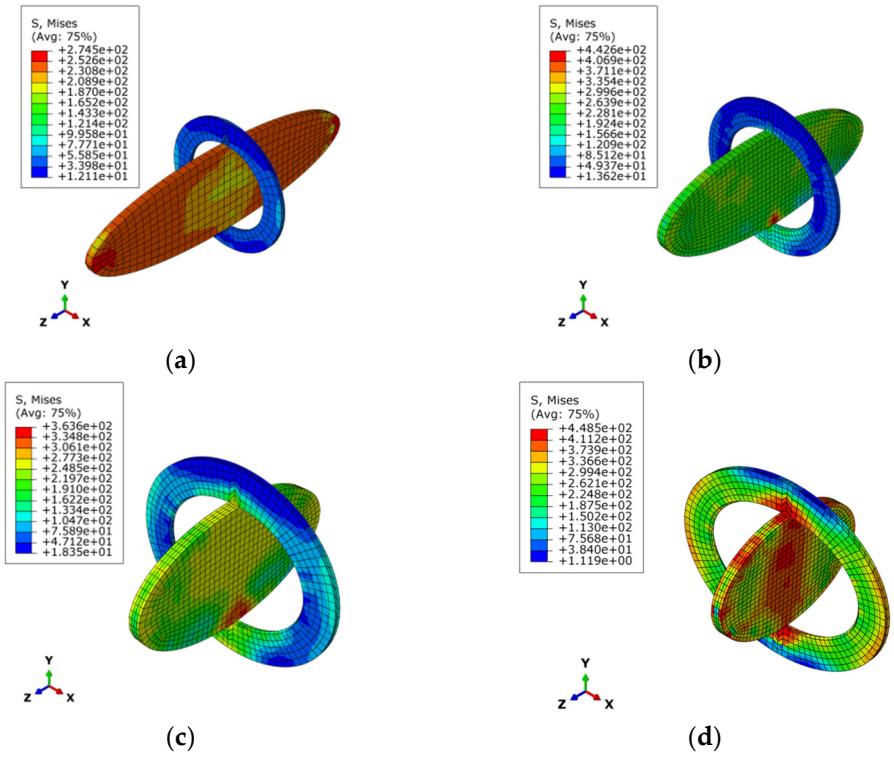
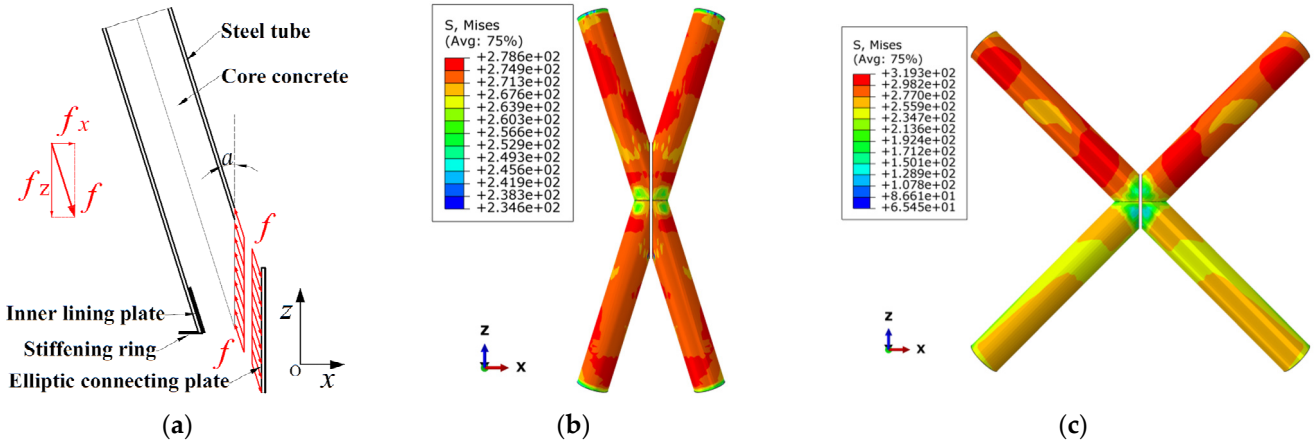


Figure 10. Local von Mises stress diagram of oblique angle specimen: (**a**) oblique angle is 35°, (**b**) oblique angle is 50°, (**c**) oblique angle is 70°, and (**d**) oblique angle is 90°.

As shown in Figure 11a, the load on the surface of the connecting plate is mainly divided into *x*-axis and *z*-axis directions. When the oblique angle becomes larger, the load component *fx* in the *x*-axis direction also becomes larger, and *f* is the pressure on the connecting plate from the steel pipes and core concrete. When the connecting plate is squeezed in the *x*-axis direction, the connecting plate is deformed along the zoy plane due to the Poisson effect and is constrained by the reinforcing ring so that the stress and deformation at the contact position between the connecting plate and the reinforcing ring are large. The larger the oblique angle is, the smaller the intersection area along the zoy plane will be, so the area and volume of the connecting plate will be reduced, which is one of the reasons for its larger stress. In addition, according to Table 4, the smaller the oblique angle, the larger the ductility coefficient, and the better the ductility.



(**a**) (**b**) (**c**)

Figure 11. Force diagram and von Mises stress of some test pieces: (**a**) 1/4 connecting plate, (**b**) oblique angle is 35°, and (**c**) oblique angle is 90°.

Figure 11b,c shows the overall von Mises stress diagram of some specimens. Through comparison, it can be seen that the stress distribution of the specimen with a small oblique angle is uniform. There is a large von Mises stress value on both the steel tube 400 mm from the end and the steel tube on the inner side of the oblique steel tube above the node. The stress distribution of upper and lower extremity steel tubes is close to *xoy* plane symmetry. However, the specimens with a large oblique angle show up-and-down asymmetry. This was mainly due to the large von Mises stress and deformation of the connecting plates and reinforcing rings mentioned above, which could not provide enough constraints on the steel tubes and recycled concrete at the node locations, resulting in poor force transmission, and the steel tubes at the lower extremity could not provide full play to the material properties, which cannot provide sufficient constraints to the steel pipe and recycled concrete at the node position, resulting in poor force transmission and the lower limb steel pipe being unable to fully exert its material properties. It can be seen that node parameter setting is crucially important for oblique grid systems. According to the analysis of the above load–displacement curve, the main reason for the lower ultimate load and poor ductility of the specimen with the larger oblique angle is that the von Mises stress and deformation of the connecting plate and the reinforcing ring at the node are large, which cannot provide enough constraints to the steel pipe and recycled concrete at the node.

6.2. Thickness of Reinforcing Ring

Figure 8b shows the load–displacement curve of the reinforced ring thickness specimen group. The load–displacement curve of this group of specimens has a similar evolution law, and the thickness of the reinforced ring has little influence on the initial stiffness, ultimate load, and residual load of the specimen. It has an effect on the evolution process of lateral displacement, as shown in Figure 9b. When the thickness of the strengthening ring is 5 mm, the out-of-plane displacement begins to occur when the axial displacement is 0.2 mm. The

specimens with a thickness of 0 mm and 5 mm begin to increase sharply when the axial displacement is 8 mm, and the specimens with a thickness of 5 mm show nonlinear growth, resulting in excessive out-of-plane displacement buckling failure.

The nephogram of von Mises stress and equivalent plastic strain in the reinforcing ring of specimens with different reinforcing ring thicknesses is shown in Figure 12. It can be seen from the figure that the maximum von Mises stress of the reinforcing ring of the specimen with a thickness of 5 mm is 273.8 MPa, which has reached the yield stress, while the plastic deformation area is the welding position between the reinforcing ring and the left and right steel pipes. A large area of plastic deformation occurs in both the connecting plate and the lining plate. Compared with the specimen with a thickness of 0 mm, the plastic deformation distribution is relatively uniform. The plastic region of the specimen, with a thickness of 0 mm, is mainly on one side of the connecting plate. The whole section of the reinforcing ring of the specimen with a thickness of 10 mm is still in the elastic stage, and its von Mises stress is far less than the yield stress. To sum up, the reinforcing rings of specimens with a thickness of 5 mm and 10 mm still have a large degree of strength surplus. However, in view of the insufficient lateral resistance of the specimen with a thickness of 5 mm, it is suggested that the reinforced ring with a thickness of 10 mm be used as the restraint member at the node of the oblique grid.

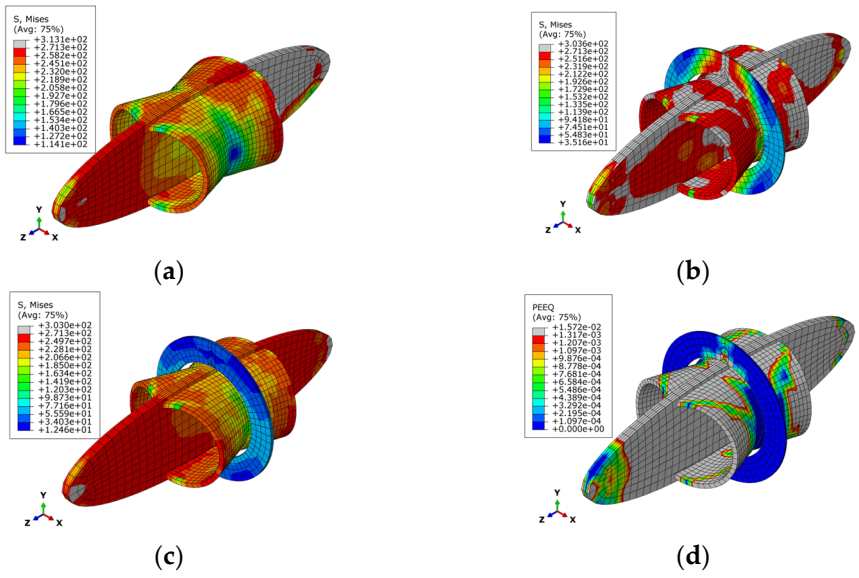


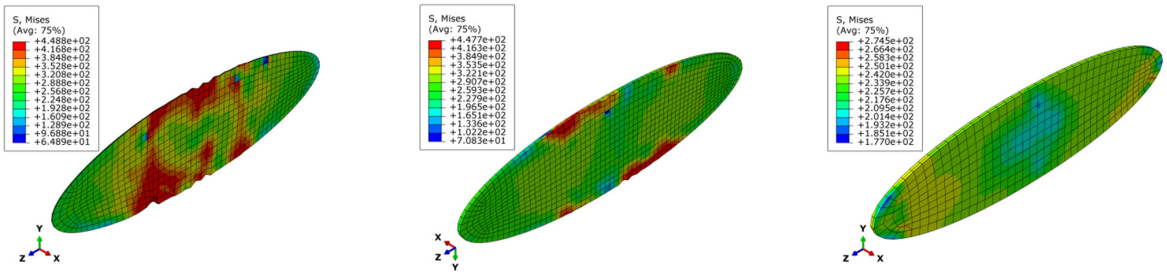
Figure 12. Von Mises stress and equivalent plastic strain: (**a**) stiffening ring thickness = 0 mm, (**b**) stiffening ring thickness = 5 mm, (**c**) stiffening ring thickness = 5 mm (PEEQ), and (**d**) stiffening ring thickness = 10 mm.

6.3. Thickness of Connecting Plate

Figure 8c shows the load–displacement curve of the connecting plate thickness specimen group. The load–displacement curve of this group of specimens has a similar evolution of l4,000 kN·aw. The connecting plate thickness has little effect on the initial stiffness of members, but the stiffness of each specimen begins to show inconsistency after reaching 4000 kN. The specimen with a connecting plate thickness of 5 mm enters the yield stage prematurely. The specimen's ultimate load increases as the connecting plate's thickness increases. It can be seen from Figure 9c that when the thickness of the connecting plate is 10 mm, the out-of-plane displacement of the specimen is well controlled, and the displacement value is within the interval (−3 mm, 2 mm). When the thickness of the connecting plate is 5 mm, the out-of-plane displacement begins to occur when the axial displacement of the specimen is 1.3182 mm, and its curve fluctuates up and down, resulting in poor stability of the member. As can be seen from Table 4, the greater the thickness of the connecting plate, the greater the strengthening coefficient, which indicates that the thick-

ness of the connecting plate has an influence on the constraint of steel pipe to the core of recycled concrete.

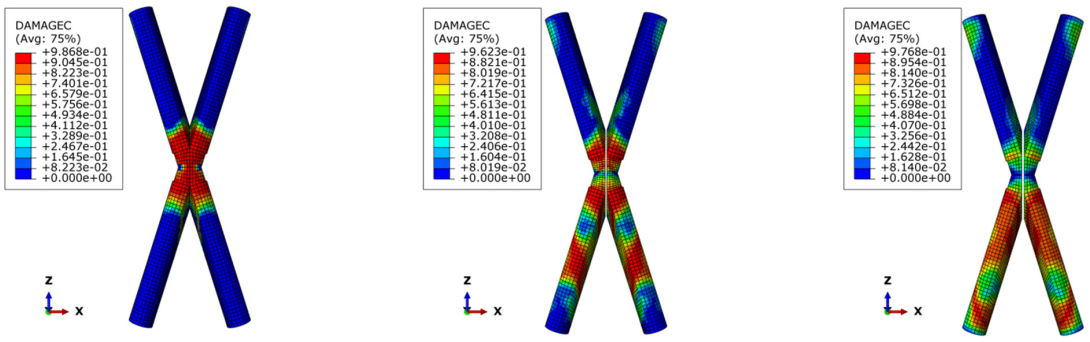
Figure 13 shows the von Mises stress nephogram of some specimens with different thicknesses of connecting plates. It can be seen from the figure that when the thickness of the connecting plate is less than or equal to 20 mm, the von Mises stress value in the local area of the elliptical connecting plate has reached the ultimate strength, mainly in the area where it contacts the oblique steel pipe. The connecting plate with a thickness of 5 mm, in particular, has obvious deformation, indicating that it can no longer bear the load and provide effective lateral restraint for recycled concrete.



(**a**) (**b**) (**c**)

Figure 13. Von Mises stress nephogram: (**a**) thickness of connecting plate = 5 mm, (**b**) thickness of connecting plate = 20 mm, and (**c**) thickness of connecting plate = 28 mm.

Figure 14 shows the nephogram of concrete compression damage. It can be seen from the figure that the distribution law of recycled concrete compression damage is different for specimens with different connection plate thicknesses. The compression damage of specimens with 5 mm connection plate thickness is mainly concentrated in the node area, and the damage value reaches the peak value of 0.9868. It shows that the recycled concrete at the node position cannot be effectively restrained and is the first to be destroyed, which does not meet the failure criterion of "non-node zone is destroyed before node zone". The compressive damage of specimens with 20 mm connection plate thickness is distributed not only in the node area but also in the middle of the lower limb concrete of members. However, the concrete in the node area is damaged first, and it does not meet the failure criterion of "non-node zone is destroyed before node zone"; its damage value is less than 5 mm, which indicates that the connection plate with this thickness can provide better restraint. The compressive damage of the specimens with a thickness of 28 mm is mainly distributed in the lower limb concrete but rarely distributed in the node area, which meets the failure criterion of "non-node zone is destroyed before node zone". In conclusion, the thickness of the connecting plate has an influence on the constraining effect of the concrete in the node area and the failure location of the construction.



(**a**) (**b**) (**c**)

Figure 14. Nephogram of concrete compression damage: (**a**) thickness of connecting plate = 5 mm, (**b**) thickness of connecting plate = 20 mm, and (**c**) thickness of connecting plate = 28 mm.

6.4. Concrete Strength

Figure 8d shows the load–displacement diagram of specimen groups with different concrete strengths. The ultimate load and initial stiffness of the specimen are proportional to the concrete strength. The specimen with lower concrete strength has a gentle descending section after the ultimate load. The curve of the specimen with 30 MPa concrete strength is nearly parallel to the x-axis after the peak load, and the difference between the residual load and the ultimate load is small. On the contrary, the descending section of the specimen with high concrete strength shows non-uniformity. For example, the specimen with 100 MPa strength has two "sudden drops", with displacements of around 16 mm and 27 mm, respectively, and the specimen with 80 MPa strength has a similar phenomenon.

As can be seen from Figure 15, the ductility coefficient and strength improvement coefficient increase inversely with the strength of concrete, which is mainly related to the brittleness of high-strength concrete. Secondly, the high strength of the concrete leads to the failure of the steel tube to provide effective lateral restraint, and the restraint effect of core concrete in the node area is insufficient. This shows that when setting the parameters of an oblique grid, the combination of steel tube and recycled concrete can be brought into play only by selecting the appropriate constraint coefficient and hoop index.

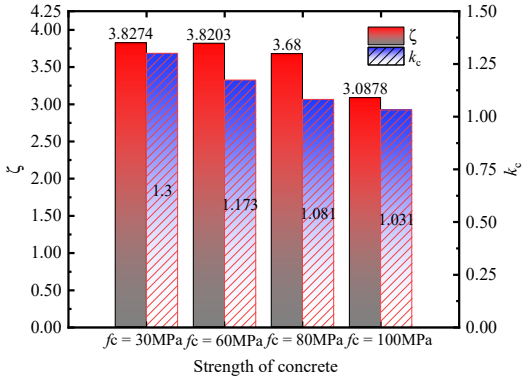


Figure 15. Relevant parameters of specimen groups with different concrete strengths.

Figure 9d shows the displacement–lateral displacement diagram of specimen groups with different concrete strengths. The lateral displacement of specimens with higher concrete strengths fluctuates greatly, while the lateral displacement of specimens with 30 MPa strengths develops slowly. The first reason is that its ultimate load is small, and the specimen will be destroyed without large lateral deformation. The second reason is that concrete with lower strength has better ductility. The axial displacement corresponding to the initial lateral displacement of the specimen with the strength of 100 MPa is only 6.0 mm, which is earlier than that of the other specimens, which is also caused by the high brittleness of the concrete inside and the lack of constraints on the concrete members.

In ABAQUS, PEEQ represents the equivalent plastic strain, which is the accumulation result of plastic strain in the whole deformation process and the sum of the absolute values of plastic strain in the processes of tension and compression. When PEEQ has a numerical value, it indicates that the position has reached yield and entered the plastic stage. It can be seen from Figure 16 that when the concrete strength is between 30 MPa and 60 MPa, the PEEQ value of the restrained steel parts at the nodes is still small, and only plastic deformation occurs in some areas of the elliptic connecting plate. The stress concentration is formed at the edge of its position along the long axis, and the area is small, which can still provide a good restraining effect on the recycled concrete at the nodes and can reach the criterion of "non-node zone is destroyed before node zone" when members are destroyed. When the concrete strength is between 80 MPa and 100 MPa, the PEEQ value of the restrained steel parts is large, plastic deformation occurs in a large area of the elliptical connecting plate and the inner lining plate, and the strain value is large, which further

proves the phenomenon that the steel pipe cannot provide effective circumferential restraint due to the high concrete strength.

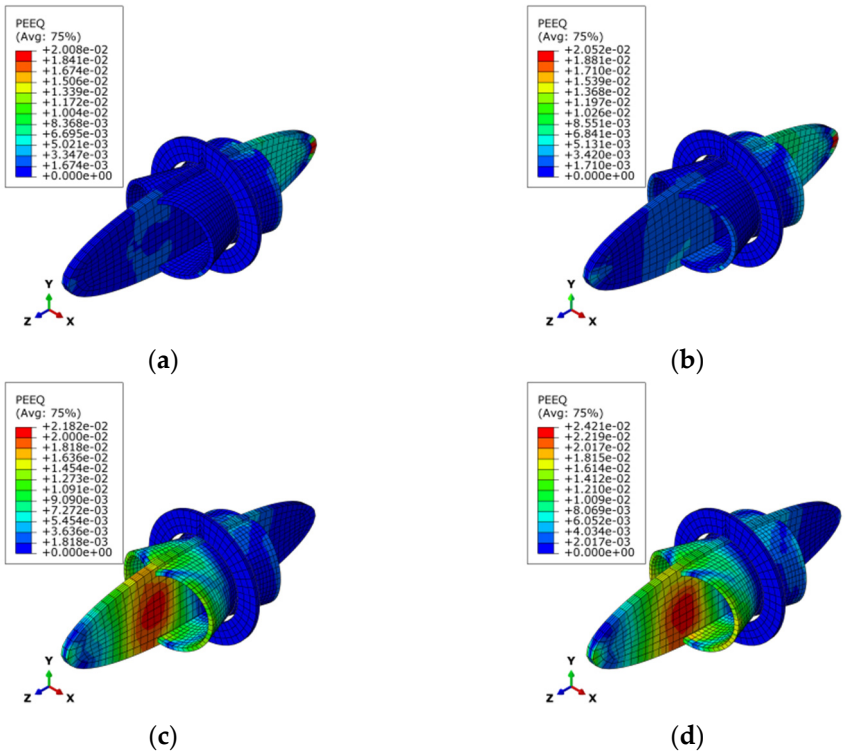


Figure 16. PEEQ diagram of node steel parts: (**a**) f_c = 30 MPa, (**b**) f_c = 60 MPa, (**c**) f_c = 80 MPa, and (**d**) f_c = 100 MPa.

6.5. Recycled Aggregate Replacement Rate

Figure 8e shows the load–displacement diagram of specimen groups with different replacement rates of recycled aggregate. The ultimate load of a specimen is inversely proportional to the replacement rate of recycled aggregate. The specimen with a 100% replacement rate has a different curve evolution law from other specimens, and the displacement corresponding to its peak load has hysteresis, which is mainly due to the performance defects of a large number of cracks generated in the crushing process of recycled concrete. Therefore, a large axial compression displacement is needed to make the cracks of the aggregate close and bear the force continuously. Furthermore, the load–displacement curves of concrete, except for the replacement rate of 100%, have good ductility and a gentle and uniform decline section. Secondly, it can be seen from the displacement–lateral displacement in Figure 9e that the aggregate replacement rate has no obvious regularity in the development and evolution of lateral displacement. The specimen with a replacement rate of 0 has lateral deformation when the axial displacement is 15 mm, and its maximum lateral displacement is only 1.123 mm, which has relatively good lateral resistance. As can be seen from Table 4, the replacement rate of recycled aggregate has an impact on the energy dissipation capacity of the specimen, and the energy dissipation factor decreases with the increase in the replacement rate of recycled aggregate. This indicates that the energy dissipation capacity decreases with the increase in the regenerated bone replacement rate, which is also due to the performance defects of the regenerated concrete with its high replacement rate and high brittleness.

Figure 17 shows the lateral displacement nephogram of the recycled aggregate replacement rate specimen group. It can be seen from the figure that when the replacement rate is 0, the main failure mode of the specimen is steel pipe buckling failure, and the buckling location is the node of the lower extremity steel pipe and the middle of the lower extremity non-node steel pipe. The samples with a replacement rate of 30%, 50%, and

70% also showed drum failure. Except for the same drum failure position as those with a replacement rate of 0, large drum failures occurred at the upper and lower column feet. However, the drum failure sequence of the above components was a non-node zone followed by a node zone, so it can be considered that the specimens met the failure criterion of "non-node zone is destroyed before node zone". The failure modes of the specimen with a 100% replacement rate are buckling failure and lateral instability failure, and the shape of the specimen after failure is close to a reverse "S" type. It shows that the replacement rate of recycled aggregate has an influence on the failure position and failure mode of members, and the lateral stiffness of members with a 100% replacement rate is insufficient, so it is not recommended in engineering practice.

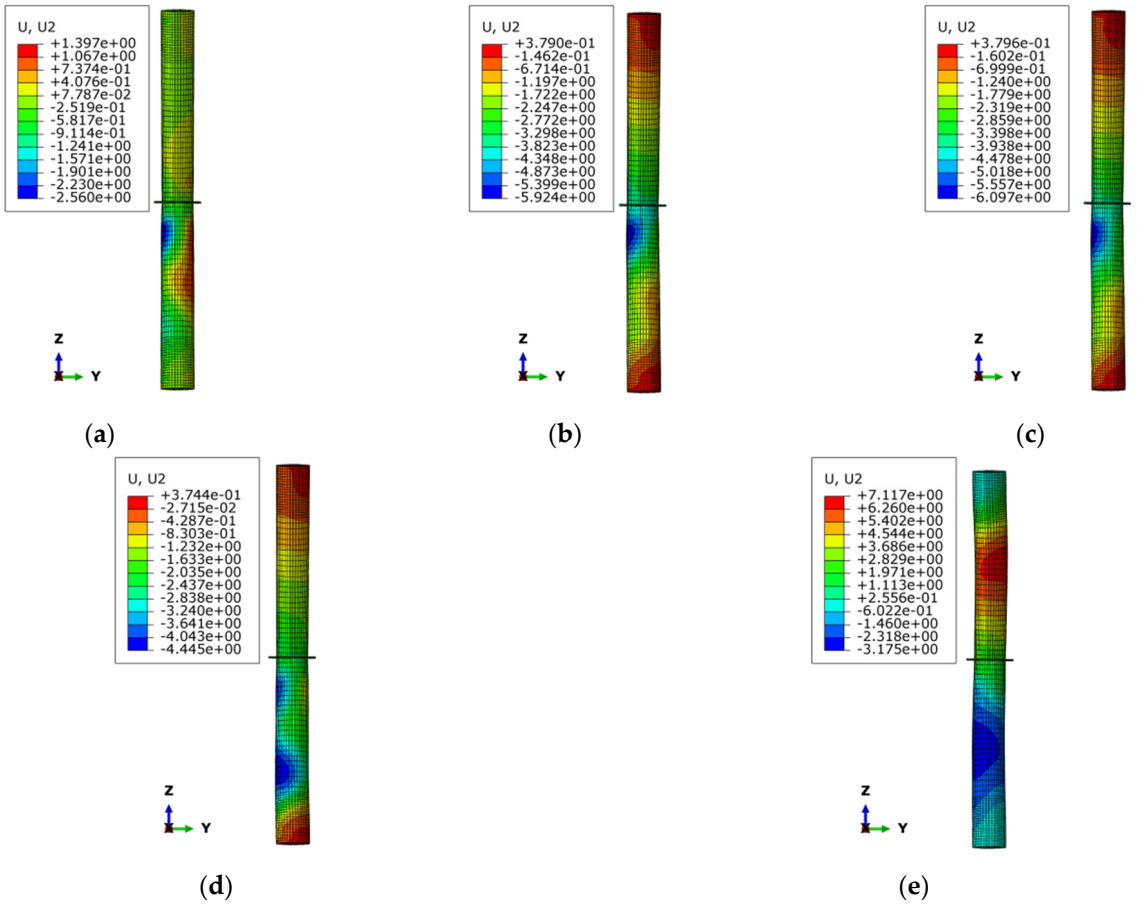


Figure 17. Lateral displacement nephogram of recycled aggregate substitution rate specimen group: (**a**) replacement rate = 0%, (**b**) replacement rate = 30%, (**c**) replacement rate = 50%, (**d**) replacement rate = 70%, and (**e**) replacement rate = 100%.

6.6. Steel Fiber Content

Figure 8f shows the load–displacement curve of the steel fiber content specimen group. It can be seen from the figure that the load–displacement curve of this group of specimens has a similar evolution law. The ultimate bearing capacity of the specimen with 2% steel fiber content is increased by 6.25% compared with that of the specimen with 0% steel fiber content, and the fiber content is directly proportional to the ultimate bearing capacity. In the RAC load–displacement curve, the slope of the load–displacement curve in the elastic section increases with the increase in fiber content. It shows that the fiber content has a great influence on the initial stiffness of the node. From the displacement–lateral displacement Figure 9f, it can be seen that the specimens with small fiber contents (0%, 0.5%, or 1.0%) will have lateral deformation when the axial displacement is 7.5 mm. From Table 4, it can be seen that the reinforcement coefficient is proportional to the steel fiber

content, indicating that the toughening effect of steel fiber has a favorable influence on the properties of the specimens. However, in engineering applications, when the volume of fiber content exceeds 2%, the bearing capacity of specimens decreases due to the easy clumping of steel fiber and the poor workability of concrete [54]. The larger the volume of steel fiber content, the greater the decline, so the content of steel fiber should not be greater than 2%.

Figure 18 shows the von Mises stress nephogram of recycled concrete with different fiber content, and the maximum von Mises stress of the specimen with 0% fiber content is smaller, which indicates that the strength of recycled concrete is significantly improved by adding fiber. The results show that the recycled concrete in the node area of all the specimens has large von Mises stress, and the stress distribution is uniform and symmetrical. The main performance is that the maximum stress occurs at the end of the far elliptical connecting plate, while the area of the area is small, which indicates that the restriction of the lining plate, elliptical connection plate, and reinforcing ring have a favorable effect on the concrete restraint in the node area, and the steel fiber has little effect on the stress distribution. Generally speaking, the force transfer mechanism of the member is reasonable and meets the requirements of node design and construction.

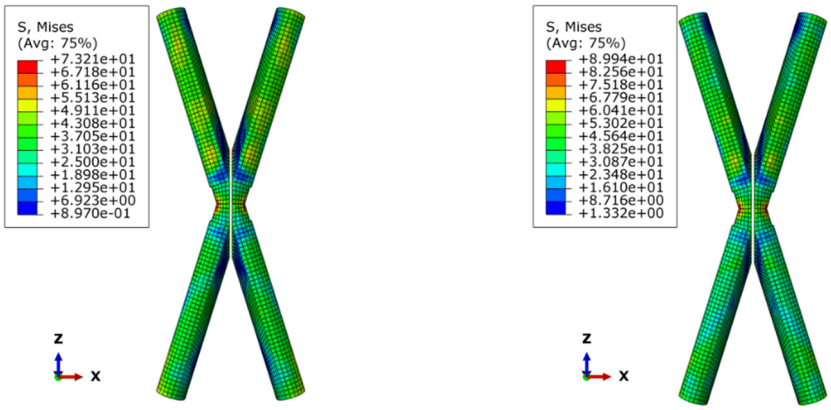


Figure 18. Von Mises stress of recycled concrete of some specimens with different fiber content: (**a**) content is 0% and (**b**) fiber content is 2%.

7. Feasibility Analysis of OGSFRCIN

7.1. Monotonic Axial Compression Performance

This chapter analyzes the feasibility of OGSFRCIN (A35-H14-L28-R30-r2.0-C60) and compares its mechanical properties with OGOCIN (A35-H14-L28-R0-r0.0-C60). According to the data of the comparison group in Table 4 and the parameters of the inclined grid nodes of OGSFRCIN and OGOCIN, as shown in Figure 19, the ultimate load of OGSFRCIN is 98.582% of the ultimate load of OGOCIN, and there is little difference between the energy dissipation factor and the ductility coefficient, indicating that the energy dissipation capacity and ductility of OGSFRCIN are not much different from those of OGOCIN. The maximum lateral displacement of OGSFRCIN is slightly larger than that of OGOCIN, but the value is still small, and the difference is negligible. It shows that the toughening effect of steel fiber and the constraining effect of outer steel pipes and node-constricting steel parts can offset the defects in the mechanical properties of recycled concrete. The OGSFRCIN also has good energy dissipation capacity and ductility.

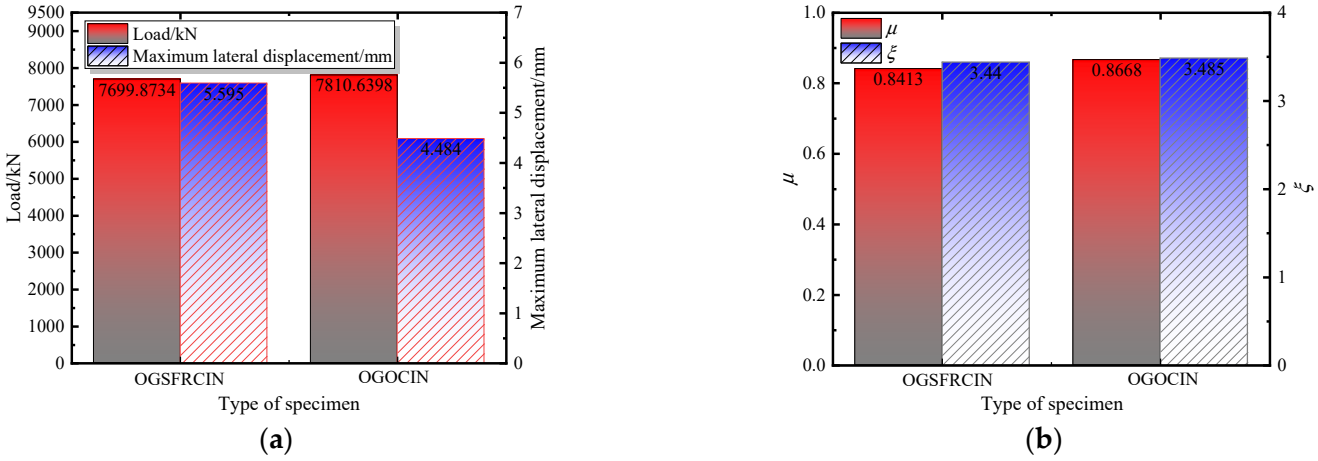


Figure 19. Comparison of parameters between OGSFRCIN and OGOCIN: (**a**) load and maximum lateral displacement and (**b**) energy dissipation and ductility coefficient.

Figure 20 shows the von Mises stress nephogram of OGSFRCIN and OGOCIN. In order to more directly reflect its deformation, the deformation amplification factor is set to 2. From the figure, the failure location of the two types of members is steel pipes in the non-node area, and the failure mode is buckling failure. According to the cloud chart of concrete compression damage, it can be seen that the compressive damage of the two types of members is mainly concentrated in the concrete in the non-node area. The tensile damage is mainly concentrated in the inner area of the non-joint area near the joint area, indicating that the concrete in this area is under great tensile action, but the overall damage value is evenly distributed, and there is no phenomenon of excessive value in a certain area. It shows that the two types of concrete can form a good interaction with the oblique grid nodes and steel tube, and both meet the failure criterion of "non-node zone is destroyed before node zone".

7.2. Seismic Performance

The mechanical properties of OGSFRCIN and OGOCIN under axial tensile and compressive reciprocating loads were analyzed. Loading regime and material constitutive are shown in Figures 21 and 22, respectively. The axial compression and axial tension increased successively with a gradient of 5 mm and 2.5 mm, respectively.

Figure 23 shows the comparison of the seismic performance of the two types of members. It can be seen from Figure 23a that the hysteretic curves of the two types of members are close to coincide and have similar evolution rules, and the hysteretic curves have a high degree of fullness, indicating that the two types of members have better energy dissipation capacity. The hysteretic curves of both are asymmetrical because the load in axial compression is jointly borne by steel pipe and concrete, while the load in axial tension is mainly borne by steel pipe, and the tensile capacity of concrete is negligible. OGSFRCIN have a higher initial stiffness than OGOCIN, but the difference is small, as shown in Figure 23b. However, the stiffness decreases rapidly in the later cycle, indicating that the latter has better ductility. In conclusion, OGSFRCIN also has good mechanical properties and rules similar to OGOCIN, which can be applied in engineering practice.

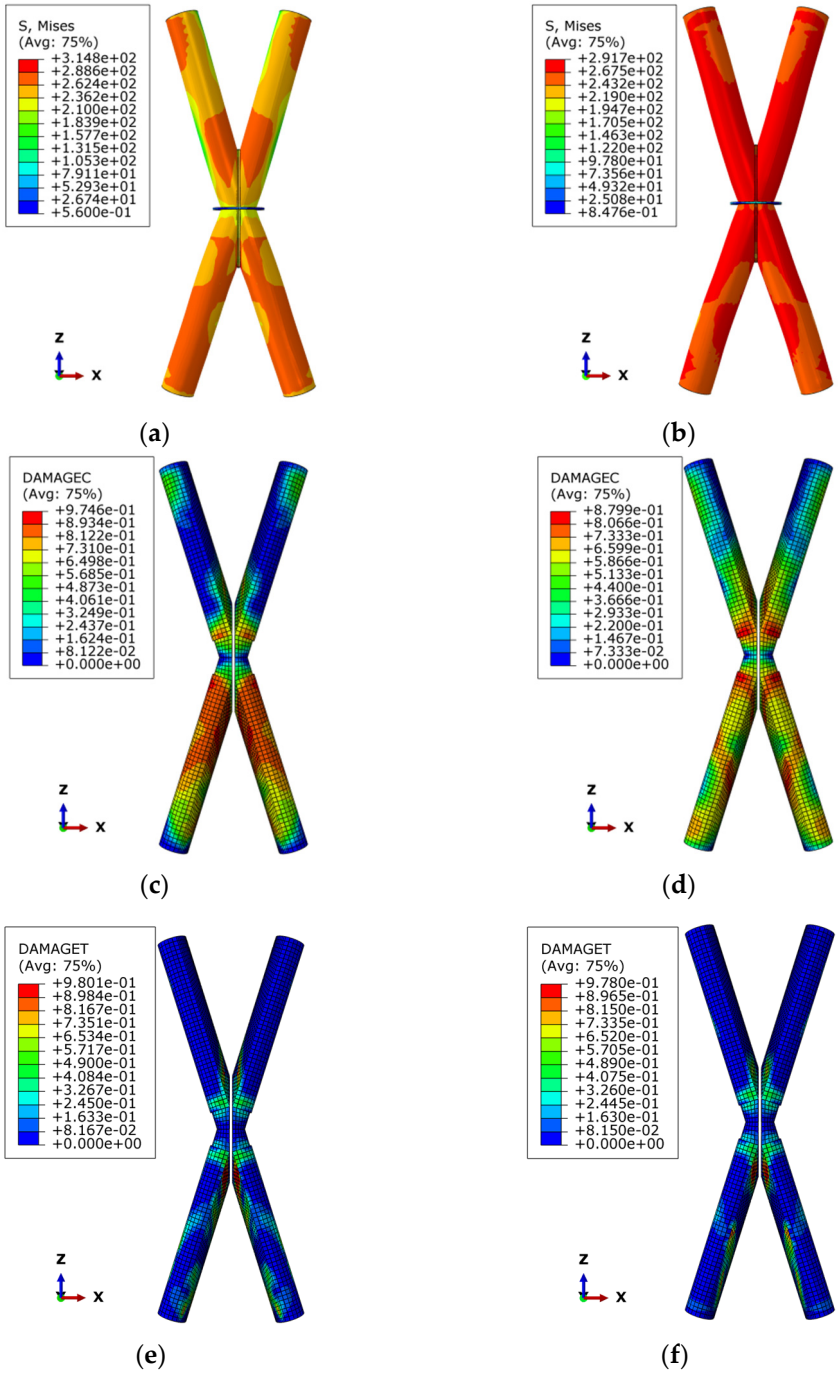


Figure 20. Cloud chart comparison of oblique grid nodes members of different concrete categories: (**a**) von Mises stress of OGSFRCIN, (**b**) von Mises stress of OGOCIN, (**c**) DAMAGEC of OGSFRCIN, (**d**) DAMAGEC of OGOCIN, (**e**) DAMAGET of OGSFRCIN, and (**f**) DAMAGET of OGOCIN.

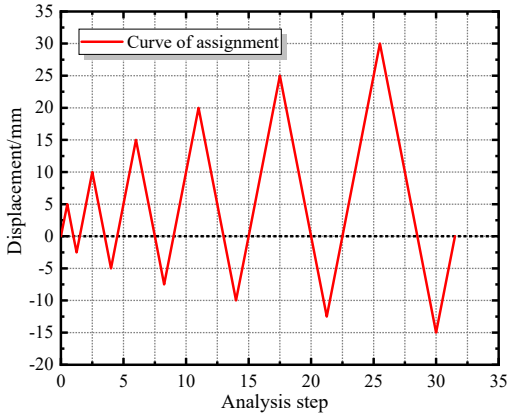


Figure 21. System of loading.

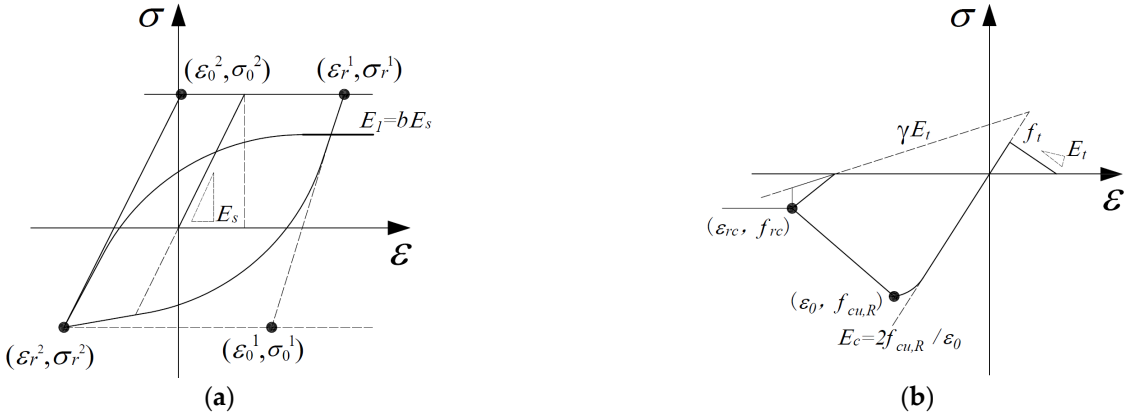


Figure 22. (**a**) Steel hysteretic constitutive and (**b**) concrete hysteretic constitutive. Note: σ_r and ε_r are the stress–strain at the reverse point, σ_0 and ε_0 are the stress–strain at the intersection of two asymptotes, and E_s, E_1, and b are the elastic modulus, plastic modulus, and hardening coefficient of steel, respectively. γ is the hysteretic characteristic parameter, E_t is the unloading stiffness of the tensile section, f_t is the tensile strength of the concrete axis, ε_{rc} is the ultimate compressive strain of concrete-filled steel tube, f_{rc} is the ultimate compressive stress of concrete-filled steel tube, ε_0 is the peak strain corresponding to the compressive strength of the recycled concrete axis, and $f_{cu,R}$ is the compressive strength of the recycled concrete axis.

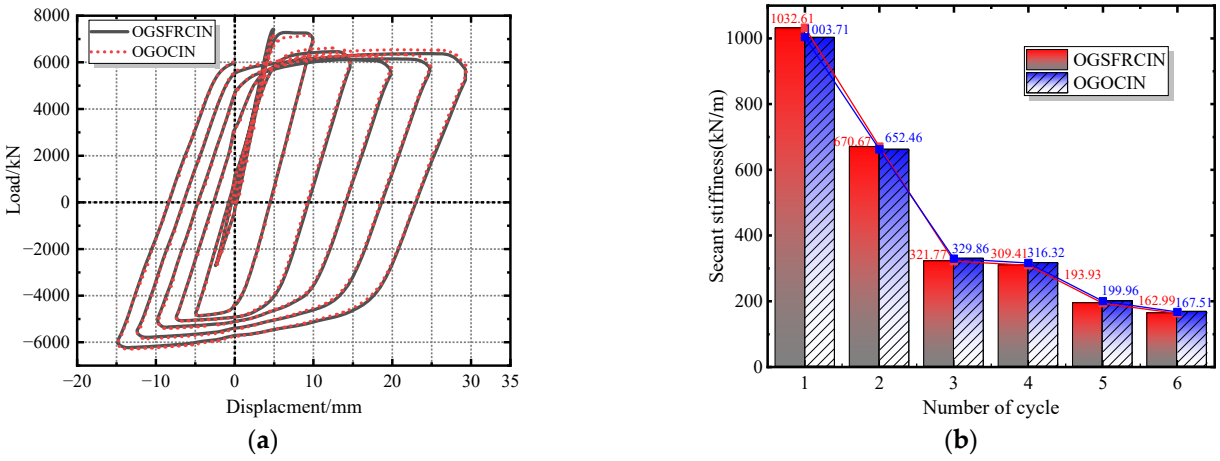


Figure 23. Comparison of seismic performance: (**a**) hysteresis curve and (**b**) secant stiffness degradation.

8. Theoretical Bearing Capacity of OGSFRCIN

Based on the symmetry of the nodes, 1/4 nodes are taken into account, and the cross-sectional areas of steel tubes, lining plates, core concrete, and connecting plates in the node area vary with height [55]. As shown in Figure 24, the section in the figure is the place where the distance from the intersection starting point is L.

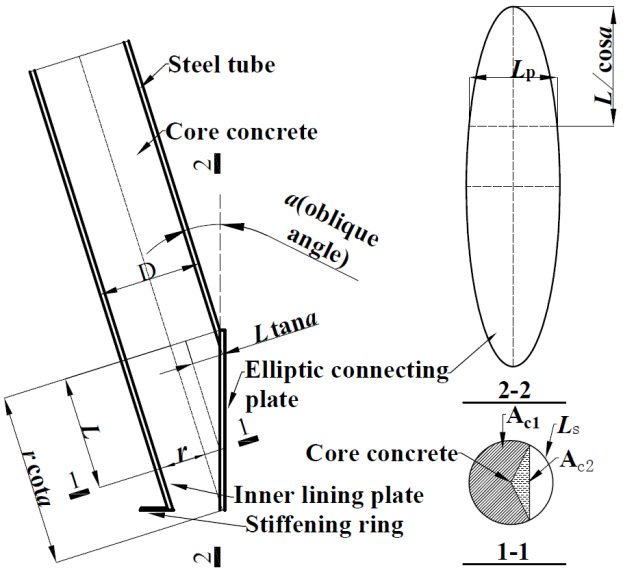


Figure 24. Schematic diagram of relevant section dimensions for bearing capacity calculation: "1" and "2" represent 1-1 and 2-2 sections, respectively.

In Figure 24, each parameter is calculated as follows:

$$A_c = A_{c1} + A_{c2}, \tag{20}$$

$$A_{c1} = r_1(\pi - \arccos x); A_{c2} = x\left(1 - x^2\right)^{0.5}, \tag{21}$$

$$A_s = L_s t_s; A_p = L_p t_p, \tag{22}$$

$$L_s = 2r_1(\pi - \arccos x)t_1; L_p = 2r_1\left(1 - x^2\right)^{0.5}, \tag{23}$$

$$x = \frac{(r_1 - L\tan a)}{r_1}, \tag{24}$$

where A_s is the section area of the outer steel pipe, A_p is the section area of the elliptic connecting plate, A_c is the section area of concrete, t_s Is the sum of wall thickness and lining thickness of steel pipe in node area, and t_p is the thickness of the elliptical connecting plate. Considering the constraint effect of an elliptical connecting plate and an inner lining plate on recycled concrete, a formula that can reflect the constraint effect coefficient is introduced [55]:

$$N_u = f_{cu,R}A_c\left(1 + \sqrt{\frac{A_s f_y}{A_c f_{cu,R}}} + \frac{A_s f_y}{A_c f_{cu,R}}\right) + \left(0.07\frac{A_s}{A_e} + 1.02\right)f_y A_e. \tag{25}$$

When calculating the cross-sectional area, the cross-section at $D/6$ from the middle cross-section of the node is used, and D is the outer diameter of the steel pipe.

Because Equation (25) is only applicable to common concrete oblique grid nodes, the constraint effect of the lining board is not considered (r_1 in Equation (23) in the literature [55] is the inner diameter of the steel pipe, etc., and the thickness of the lining plate is not

considered.).Therefore, SPSS data analysis software was used to fit and modify the formula based on the ultimate bearing capacity data in Table 4. The result is shown in Equation (26):

$$N_u{}^* = N_{sp}[k_1A + k_2H + k_3L + k_4R + k_5U + k_6C + \varpi]^2, \quad (26)$$

where A is the oblique angle, H is the thickness of the reinforcing ring (mm), L is the thickness of the connecting plate (mm), R is the replacement rate of recycled aggregate (%), U is the steel fiber content (%), and C is the cubic compressive strength of concrete (MPa). The undetermined coefficient is shown in Equations (27)–(29):

$$k_1 = -1.67 \times 10^{-4}; k_2 = -1.922 \times 10^{-3}; k_3 = 2.42 \times 10^{-3}, \quad (27)$$

$$k_4 = -2.16 \times 10^{-4}; k_5 = -2.227 \times 10^{-3}; k_6 = -4.34 \times 10^{-4}, \quad (28)$$

$$\varpi = 0.938103 \quad (29)$$

Comparing the calculated value of the theoretical ultimate bearing capacity with that of the finite element model, as shown in Figure 25, it is clear that the two values are in good agreement. This shows that the formula is correct and that it can be used to estimate the ultimate bearing capacity of this node.

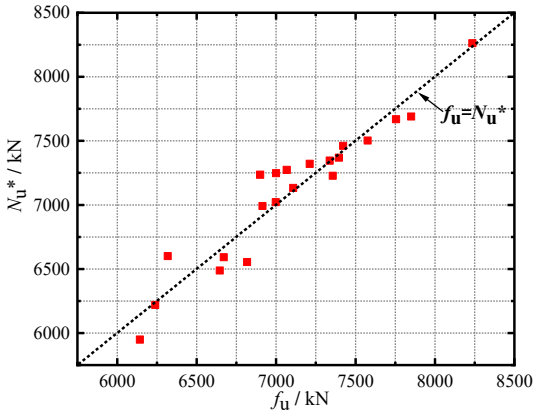


Figure 25. Comparison between theoretical value and finite element model value.

9. Conclusions

This paper is the first time OGSFRCIN, which combines steel fiber, recycled concrete, and outer steel pipe, has been put forward. To verify its feasibility, ABAQUS finite element software was used to consider the influence of six parameters, namely oblique angle, recycled aggregate replacement rate, steel fiber content, concrete strength, reinforcing ring thickness, and connecting plate thickness. The mechanical properties of this node under axial pressure were studied, and the mechanical properties of this node and OGOCIN under axial compressive load and axial seismic load were compared. The existing ultimate bearing capacity formula was modified by multi-parameter fitting, and the following conclusions were drawn:

The ABAQUS three-dimensional solid model proposed in this paper can effectively reflect the interaction between the parts of OGSFRCIN. The constitutive model of regenerated concrete with curvature coefficient, considering the effect of the regenerated aggregate substitution rate, is in good agreement with the experimental results.

The specimen's ultimate load and ductility coefficient are inversely correlated with the oblique angle. Steel tubes experience increased deformation and internal force asymmetry, as well as large von Mises stress and plastic deformation at the nodes of specimens with large oblique angles. The thickness of the reinforcement ring has little influence on the specimen's initial stiffness, ultimate load, and residual load. It has an effect on the lateral

displacement evolution process; the lateral displacement of the specimen with a thinner reinforcement ring increases nonlinearly. The thickness of the connecting plate is positively correlated with the ultimate load of the specimens. The compressive damage distribution of reclaimed concrete with different thicknesses of connecting plates is different, which has an influence on the constraining effect of concrete in the node area and the failure location of the member. The connecting plate's thickness is proportional to the specimen's ultimate load, and it influences the restraint effect of the node area's concrete as well as the member's failure position.

The ductility and strength improvement coefficients increase inversely with concrete strength, and the descending section of the load–displacement curve of specimens with high concrete strength is non-uniform. To play the combined role of steel pipe and recycled concrete, an appropriate constraint coefficient and hoop index should be selected when setting oblique mesh parameters. The recycled aggregate replacement rate has an impact on the failure location and mode of the component. The larger the replacement rate, the smaller the energy dissipation capacity. Moreover, the lateral stiffness of members with a 100% replacement rate is insufficient, so it is not recommended in engineering practice. The fiber content has a great influence on the initial stiffness of the node, which is proportional to the ultimate load and strengthening coefficient of the member. The specimens with small fiber contents have lateral deformation when the loading displacement is small. The toughening effect of steel fiber has a favorable effect on the performance of the specimens. In engineering applications, the fiber content should not be greater than 2.0%.

The stress distribution of OGSFRCIN is uniform and symmetrical from top to bottom, The lining plate, elliptical connecting plate, and reinforcing ring have an effective constraint effect on recycled concrete in the node area, and the force transmission mechanism is reasonable. OGSFRCIN also has good mechanical properties and laws similar to OGOCIN and has favorable axial compression and seismic performance. It meets the requirements of node design and construction and can be applied in engineering practice.

The modified formulas for calculating the bearing capacity of OGSFRCIN are put forward. The theoretical values are in good agreement with the finite element model values, which can provide a reference for further research.

In practical applications, the connecting plate and strengthening ring at the joints of specimens with large oblique angles should be strengthened, i.e., the steel strength or thickness should be increased. An appropriate hoop index should be selected when improving the strength of concrete, components with a replacement rate of 100% should not be used, and the fiber content should not be greater than 2.0%. In addition, the finite element modeling method and bearing capacity calculation formula in this paper can be used to evaluate and predict the mechanical properties and failure modes of the joints during structural design. Since spatial intersecting nodes are not involved in this paper, four intersecting concrete-filled steel tubular columns have included angles in both plane and space, in future studies, influences of spatial intersecting angles, out-of-plane constraints, and different loading modes can be added to improve the research content.

Author Contributions: Conceptualization, J.Z. and B.Y.; methodology, Y.Z.; software, F.W.; validation, J.Z. and B.Y.; formal analysis, F.W.; investigation, Y.Z.; resources, Y.Z.; data curation, F.W.; writing—original draft preparation, F.W.; writing—review and editing, F.W. and B.Y.; visualization, B.Y.; supervision, Y.Z.; project administration, J.Z.; funding acquisition, J.Z. All authors have read and agreed to the published version of the manuscript.

Funding: This research was funded by the National Natural Science Foundation of China, grant number [12162010].

Data Availability Statement: Data are contained within the paper.

Conflicts of Interest: The authors declare no conflict of interest.

References

1. Al-Kodmany, K. The Sustainability of Tall Building Developments: A Conceptual Framework. *Buildings* **2018**, *8*, 7. [CrossRef]
2. Elena, G. Development of high-rise buildings: Digitalization of life cycle management. *E3S Web Conf.* **2018**, *33*, 03063.
3. Fang, X.D.; Han, X.L.; Wei, H.; Ji, J.; Huang, C.; Tang, J.M. Experimental study on plannar intersecting connections used in obliquely crossing mega lattice of the Guangzhou West Tower. *J. Build. Struct.* **2010**, *31*, 56–62. (In Chinese)
4. Han, X.L.; Huang, C.; Fang, X.D.; Wei, H.; Ji, J.; Tang, J.M. Experimental study on spatial intersecting connections used in obliquely crossing mega lattice of the Guangzhou West Tower. *J. Build. Struct.* **2010**, *31*, 63–69. (In Chinese)
5. Han, X.; Huang, C.; Ji, J.; Wu, J. Experimental and numerical investigation of the axial behavior of connection in cfst diagrid structures. *Tsinghua Sci. Technol.* **2008**, *13*, 108–113. [CrossRef]
6. Guo, J.; Shi, Q.; Ma, G.; Cai, W.; Li, T.; Yang, R. Mechanical Behavior of Concrete-filled Steel Tubular Space Intersecting Nodes in High-rise Oblique Diagrid Tube Structures. *KSCE J. Civ. Eng.* **2022**, *26*, 4584–4602. [CrossRef]
7. Zhou, W.; Zhang, J.; Cao, Z. Experiment and Analysis on X-Shaped Reinforced Concrete Joint in Diagrid Structures. *ACI Struct. J.* **2013**, *110*, 51684398. [CrossRef]
8. Kim, Y.-J.; Kim, M.-H.; Jung, I.-Y.; Ju, Y.K.; Kim, S.-D. Experimental investigation of the cyclic behavior of nodes in diagrid structures. *Eng. Struct.* **2011**, *33*, 2134–2144. [CrossRef]
9. Huang, C.; Han, X.L.; Wang, C.F.; Ji, J.; Li, W.Y. Parametric analysis and simplified calculating method for diagonal grid structural system. *J. Build. Struct.* **2010**, *31*, 70–77. (In Chinese)
10. Huang, C.; Han, X.L.; Ji, J.; Xie, W.Q. Theoretical investigation into axial bearing capacity of planar intersecting connections of concrete-filled steel tube. *J. South China Univ. Technol.* **2010**, *38*, 128–134. (In Chinese)
11. Wu, D.; Yang, T.; Xiong, Y.; Tesfamariam, S. Experimental assessment on aseismic capacity of a perimeter diagrid concrete core structure: Shake table tests. *Measurement* **2022**, *203*, 111925. [CrossRef]
12. Song, S.; Zhang, C. Performance-based plastic design and seismic performance evaluation of twisted diagrids with shear links. *Struct. Des. Tall Spéc. Build.* **2022**, *31*, e1974. [CrossRef]
13. Shi, Q.; Ying, Y.; Wang, B. Experimental investigation on the seismic performance of concrete-filled steel tubular joints in diagrid structures. *Structures* **2021**, *31*, 230–247. [CrossRef]
14. Fu, Q.; Wang, X.; Dai, T. Research on Mechanical Behaviour of High-rise Diagonal Grid Tube Structure and Case study. *IOP Conf. Ser. Mater. Sci. Eng.* **2019**, *603*, 032026. [CrossRef]
15. Azari-Dodaran, N.; Ahmadi, H. Static behavior of offshore two-planar tubular KT-joints under axial loading at fire-induced elevated temperatures. *J. Ocean Eng. Sci.* **2019**, *4*, 352–372. [CrossRef]
16. Nassiraei, H. Static strength of tubular T/Y-joints reinforced with collar plates at fire induced elevated temperature. *Mar. Struct.* **2019**, *67*, 102635. [CrossRef]
17. Gao, F.; Zhu, H.; Liang, H.; Tian, Y. Post-fire residual strength of steel tubular T-joint with concrete-filled chord. *J. Constr. Steel Res.* **2017**, *139*, 327–338. [CrossRef]
18. Lie, S.; Li, T.; Shao, Y.; Vipin, S. Plastic collapse load prediction of cracked circular hollow section gap K-joints under in-plane bending. *Mar. Struct.* **2016**, *50*, 20–34. [CrossRef]
19. Wang, B.; Shi, Q.; Cai, W. Seismic behavior and damage assessment of concrete-filled steel tube columns in diagrid structures. *Struct. Des. Tall Spéc. Build.* **2021**, *31*, e1904. [CrossRef]
20. Jun, T.; Liang, G.W.; Sheng, R.B.; Hua, L.Z. Seismic Performance Research of High-Rise Diagrid Tube-Core Tube Structures. *Adv. Mater. Res.* **2010**, *163–167*, 2005–2012.
21. Jun, T.; Liang, G.W.; Sheng, R.B.; Hua, L.Z.; Jun, D.C. Research on Seismic Performance Objectives of High-Rise Diagrid Tube Structures. *Adv. Mater. Res.* **2010**, *163–167*, 1100–1106.
22. Karalar, M.; Özkılıç, Y.O.; Aksoylu, C.; Sabri, M.M.; Beskopylny, A.N.; Stel'Makh, S.A.; Shcherban, E.M. Flexural behavior of reinforced concrete beams using waste marble powder towards application of sustainable concrete. *Front. Mater.* **2022**, *9*, 1068791. [CrossRef]
23. Çelik, A.İ.; Özkılıç, Y.O.; Zeybek, Ö.; Karalar, M.; Qaidi, S.; Ahmad, J.; Burduhos-Nergis, D.D.; Bejinariu, C. Mechanical Behavior of Crushed Waste Glass as Replacement of Aggregates. *Materials* **2022**, *15*, 8093. [CrossRef] [PubMed]
24. Qaidi, S.; Najm, H.M.; Abed, S.M.; Özkılıç, Y.O.; Al Dughaishi, H.; Alosta, M.; Sabri, M.M.; Alkhatib, F.; Milad, A. Concrete Containing Waste Glass as an Environmentally Friendly Aggregate: A Review on Fresh and Mechanical Characteristics. *Materials* **2022**, *15*, 6222. [CrossRef] [PubMed]
25. Karalar, M.; Bilir, T.; Çavuşlu, M.; Özkiliç, Y.O.; Sabri, M.M. Use of recycled coal bottom ash in reinforced concrete beams as replacement for aggregate. *Front. Mater.* **2022**, *9*, 1064604. [CrossRef]
26. Zeybek, Ö.; Özkılıç, Y.O.; Karalar, M.; Çelik, A.İ.; Qaidi, S.; Ahmad, J.; Burduhos-Nergis, D.D.; Burduhos-Nergis, D.P. Influence of Replacing Cement with Waste Glass on Mechanical Properties of Concrete. *Materials* **2022**, *15*, 7513. [CrossRef] [PubMed]
27. Maedeh, H.; Mehdi, D.; Elham, A. Three-dimensional multiscale simulations of recycled aggregate concrete employing energy homogenization and finite element approaches. *Constr. Build. Mater.* **2022**, *328*, 127110.
28. Topçu, I.B.; Şengel, S. Properties of concretes produced with waste concrete aggregate. *Cem. Concr. Res.* **2004**, *34*, 1307–1312. [CrossRef]
29. Li, J.; Guo, M.Q. The Technical and Economic Analysis about Recycled Concrete. *Adv. Mater. Res.* **2011**, *374–377*, 1614–1618. [CrossRef]

30. Eguchi, K.; Teranishi, K.; Nakagome, A.; Kishimoto, H.; Shinozaki, K.; Narikawa, M. Application of recycled coarse aggregate by mixture to concrete construction. *Constr. Build. Mater.* **2007**, *21*, 1542–1551. [CrossRef]
31. Butler, L.; West, J.; Tighe, S. The effect of recycled concrete aggregate properties on the bond strength between RCA concrete and steel reinforcement. *Cem. Concr. Res.* **2011**, *41*, 1037–1049. [CrossRef]
32. Mas, B.; Cladera, A.; del Olmo, T.; Pitarch, F. Influence of the amount of mixed recycled aggregates on the properties of concrete for non-structural use. *Constr. Build. Mater.* **2012**, *27*, 612–622. [CrossRef]
33. Dong, C.; Zhang, Q.; Chen, C.; Jiang, T.; Guo, Z.; Liu, Y.; Lin, S. Fresh and hardened properties of recycled plastic fiber reinforced self-compacting concrete made with recycled concrete aggregate and fly ash, slag, silica fume. *J. Build. Eng.* **2022**, *62*, 105384. [CrossRef]
34. Bai, G.; Liu, B. Nonlinear finite element analysis of bond-slip performance of recycled aggregate concrete filled circular steel tube. *J. Adhes. Sci. Technol.* **2019**, *33*, 1294–1319. [CrossRef]
35. Yu, F.; Fang, Y.; Zhang, Y.; Xu, L.; Bai, R. Mechanical behavior of self-stressing steel slag aggregate concrete filled steel tubular stub columns. *Struct. Concr.* **2020**, *21*, 1597–1611. [CrossRef]
36. Zheng, Y.; He, D.; Yan, G.; Mbanda, E. Axial compressive behaviour of stainless steel tube-confined steel-reinforced recycled concrete stub columns. *J. Constr. Steel Res.* **2022**, *199*, 107597. [CrossRef]
37. Zhou, J.; Zhao, L.; Wang, Y.; Zhao, Q. Research on Axial Compression Performance of Waste Fiber Recycled Concrete Column. *IOP Conf. Ser. Earth Environ. Sci.* **2020**, *455*, 012089. [CrossRef]
38. Nasir, A.M.; Waqas, A.; Kaffayatullah, K.; Ayaz, A. Steel Fiber-Reinforced Concrete: A Systematic Review of the Research Progress and Knowledge Mapping. *Materials* **2022**, *15*, 6155.
39. Xu, J.X.; Xiao, J.Z.; Luo, S.R.; Zhang, Q.T. Research progress and prospect of fiber-recycled concrete. *Ind. Constr.* **2022**, *52*, 10–17+31. (In Chinese)
40. Mihai, I.C.; Jefferson, A.D.; Lyons, P. A plastic-damage constitutive model for the finite element analysis of fibre reinforced concrete. *Eng. Fract. Mech.* **2016**, *159*, 35–62. [CrossRef]
41. Wu, K.; Qian, S.; Zheng, H.; Zhou, Y.; Zhu, R. Energy dissipation and damage on the interface of steel and steel fiber-reinforced concrete composite column. *Struct. Des. Tall Spéc. Build.* **2022**, *31*, 1984. [CrossRef]
42. Su, Q. Strengths of Recycled Concrete Added with Steel Fiber. *Arch. Civ. Eng.* **2020**, *66*, 693–703. [CrossRef]
43. Zhou, J.H.; Kang, T.B.; Wang, F.C.; Dong, W. Experimental study on fracture properties of Waste fiber recycled concrete. *MATEC Web Conf.* **2016**, *63*, 03015. [CrossRef]
44. Zhang, P.; Wang, C.; Gao, Z.; Wang, F. A review on fracture properties of steel fiber reinforced concrete. *J. Build. Eng.* **2023**, *67*. [CrossRef]
45. Huang, C.; Han, X.-L.; Ji, J.; Tang, J.-M. Behavior of concrete-filled steel tubular planar intersecting connections under axial compression, Part 1: Experimental study. *Eng. Struct.* **2010**, *32*, 60–68. [CrossRef]
46. Qiu, Z.X.; Huang, J.H.; Xie, S.K.; Liu, Z.Y. Application of Shell Element in Finite Element Analysis. *Die Mould Technol.* **2003**, 9–11+15. (In Chinese)
47. Zhang, X.G.; Chen, Z.P.; Xue, J.Y.; Su, Y.Y. Test and Finite Element Analysis of Seismic Performance for Recycled Aggregate Concrete Filled Circular Steel Tube Column. *J. Basic Sci. Eng.* **2016**, *24*, 582–594. (In Chinese)
48. Yang, Y.-F.; Han, L.-H. Experimental behaviour of recycled aggregate concrete filled steel tubular columns. *J. Constr. Steel Res.* **2006**, *62*, 1310–1324. [CrossRef]
49. Tian, Y. Research on the Compressive Properties of RRACFSTSC and STCRRACSC. Master's Thesis, Guangzhou University, Guangzhou, China, 2020. (In Chinese).
50. Wang, F.C.; Zhao, J.; Liu, J.; Chen, J.; Yin, L.L.; Zhu, Y.H. Mechanical Properties of New Type Grouting Sleeves Considering Effect of Steel Bar Eccentricity. *J. Univ. Jinan* **2022**, *36*, 549–559. (In Chinese)
51. Jinjun, X.; Zongping, C.; Jianyang, X.; Yisheng, S.U. Failure mechanism of interface bond behavior between circular steel tube and recycled aggregate concrete by push-out test. *J. Build. Struct.* **2013**, *34*, 148–157. (In Chinese)
52. Zhang, X.G.; Zhou, G.Q.; Fan, Y.H.; Gao, X.; Leng, F.G. Axial compressive property of circular steel tubular stub column filled with basalt-fiber reinforced recycled-concrete. *Acta Mater. Compos. Sin.* **2023**, *40*, 369–382. (In Chinese)
53. Xu, Y.W.; Yao, J.; Li, Z.X. Cyclic axial compression tests on concrete-filled elliptical steel tubular stub columns. *J. Harbin Eng. Univ.* **2020**, *41*, 635–642. (In Chinese)
54. Zhao, Z.Q.; Zhao, J.H.; Deng, Y.J. Experimental study on axial compression performance of steel fiber recycled concrete filled square steel tube short columns. *Ind. Constr.* **2018**, *48*, 168–174. (In Chinese)
55. Huang, C. Research on Compressive Behavior of Intersecting Connection of Concrete Filled Steel Tubular Diagrid Structure. Ph.D. Thesis, South China University of Technology, Guangzhou, China, 2010. (In Chinese).

Disclaimer/Publisher's Note: The statements, opinions and data contained in all publications are solely those of the individual author(s) and contributor(s) and not of MDPI and/or the editor(s). MDPI and/or the editor(s) disclaim responsibility for any injury to people or property resulting from any ideas, methods, instructions or products referred to in the content.